Ala-Lahti, Matti; Dimmock, Andrew P.; Pulkkinen, Tuija I.; Good, Simon W.; Yordanova, Emilya; Turc, Lucile; Kilpua, Emilia K.J.

Transmission of an ICME Sheath Into the Earth's Magnetosheath and the Occurrence of Traveling Foreshocks

Published in:
Journal of Geophysical Research: Space Physics

DOI:
10.1029/2021JA029896

Published: 01/12/2021

Document Version
Publisher's PDF, also known as Version of record

Please cite the original version:
Ala-Lahti, M., Dimmock, A. P., Pulkkinen, T. I., Good, S. W., Yordanova, E., Turc, L., & Kilpua, E. K. J. (2021). Transmission of an ICME Sheath Into the Earth's Magnetosheath and the Occurrence of Traveling Foreshocks. *Journal of Geophysical Research: Space Physics*, *126*(12), Article e2021JA029896. https://doi.org/10.1029/2021JA029896

JGR Space Physics

RESEARCH ARTICLE
10.1029/2021JA029896

Transmission of an ICME Sheath Into the Earth's Magnetosheath and the Occurrence of Traveling Foreshocks

Matti Ala-Lahti[1], Andrew P. Dimmock[2], Tuija I. Pulkkinen[3,4], Simon W. Good[1], Emilya Yordanova[2], Lucile Turc[1], and Emilia K. J. Kilpua[1]

[1]Department of Physics, University of Helsinki, Helsinki, Finland, [2]Swedish Institute of Space Physics, Uppsala, Sweden, [3]Department of Climate and Space Sciences and Engineering, University of Michigan, Ann Arbor, MI, USA, [4]Department of Electronics and Nanoengineering Engineering, Aalto University, Espoo, Finland

Key Points:

- Several intervals in an interplanetary coronal mass ejection (ICME) sheath maintained their magnetic structure with transmission into the Earth's magnetosheath
- The intervals caused traveling foreshocks, ultralow-frequency fluctuations, and backstreaming ions upstream of the quasi-parallel bow shock
- Correlation of observations from a solar wind monitor and a spacecraft in the magnetosheath depends on spacecraft alignment

Correspondence to:
M. Ala-Lahti,
matti.ala-lahti@helsinki.fi

Citation:
Ala-Lahti, M., Dimmock, A. P., Pulkkinen, T. I., Good, S. W., Yordanova, E., Turc, L., & Kilpua, E. K. J. (2021). Transmission of an ICME sheath into the Earth's magnetosheath and the occurrence of traveling foreshocks. *Journal of Geophysical Research: Space Physics*, *126*, e2021JA029896. https://doi.org/10.1029/2021JA029896

Received 18 AUG 2021
Accepted 25 NOV 2021

Abstract The transmission of a sheath region driven by an interplanetary coronal mass ejection into the Earth's magnetosheath is studied by investigating in situ magnetic field measurements upstream and downstream of the bow shock during an ICME sheath passage on 15 May 2005. We observe three distinct intervals in the immediate upstream region that included a southward magnetic field component and are traveling foreshocks. These traveling foreshocks were observed in the quasi-parallel bow shock that hosted backstreaming ions and magnetic fluctuations at ultralow frequencies. The intervals constituting traveling foreshocks in the upstream survive transmission to the Earth's magnetosheath, where their magnetic field, and particularly the southward component, was significantly amplified. Our results further suggest that the magnetic field fluctuations embedded in an ICME sheath may survive the transmission if their frequency is below ~0.01 Hz. Although one of the identified intervals was coherent, extending across the ICME sheath and being long-lived, predicting ICME sheath magnetic fields that may transmit to the Earth's magnetosheath from the upstream at L1 observations has ambiguity. This can result from the strong spatial variability of the ICME sheath fields in the longitudinal direction, or alternatively from the ICME sheath fields developing substantially within the short time it takes the plasma to propagate from L1 to the bow shock. This study demonstrates the complex interplay ICME sheaths have with the Earth's magnetosphere when passing by the planet.

1. Introduction

Interplanetary coronal mass ejections (ICMEs) are massive clouds of plasma and magnetic field that originate from vast eruptions in the Sun's corona. They transfer energy in interplanetary space and are the main drivers of space weather at the Earth (e.g., Gonzalez et al., 1999, 2011; Kilpua, Balogh, et al., 2017; and references therein). An ICME consists of a magnetic ejecta which drives a shock and sheath region when traveling with supermagnetosonic speeds relative to the solar wind in interplanetary space. Interplanetary shocks, including those not associated with ICMEs, have been extensively studied (e.g., Blanco-Cano et al., 2016; Kajdič et al., 2019; Oliveira & Samsonov, 2018; Tsurutani et al., 2011). And several recent works have focused on understanding the radial evolution of ICME ejecta (e.g., Good et al., 2019; Janvier et al., 2019; Lugaz et al., 2020; Luhmann et al., 2020; Manchester et al., 2017; Scolini et al., 2018) and the sheath regions driven by ICMEs (e.g., Good et al., 2020; Moissard et al., 2019; Salman et al., 2020; Yermolaev et al., 2018). New missions, such as Solar Orbiter (Müller et al., 2013) and Parker Solar Probe (Fox et al., 2016), can improve the understanding of ICMEs by observing them closer to the Sun and earlier in their evolution (see e.g., Winslow et al., 2021).

Each of these elements of the ICME have an independent capability to disturb the plasma environments that surround the Earth (e.g., Huttunen et al., 2002; Pulkkinen et al., 2007; Tsurutani et al., 1988; Yermolaev et al., 2012; Zhou & Tsurutani, 2001). ICME sheaths have a vital contribution to most severe geomagnetic storms (Huttunen & Koskinen, 2004; Kilpua, Balogh, et al., 2017; Meng et al., 2019) and they can drive intense substorms (Tsurutani et al., 2015). An ICME sheath passage through the Earth's magnetosphere compresses the dayside magnetopause (e.g., Lugaz et al., 2016) and causes strong auroral currents in the high-latitude magnetosphere (Huttunen & Koskinen, 2004; Huttunen et al., 2002) and large geomagnetically induced currents (Dimmock et al., 2019; Huttunen et al., 2008). In addition, intense low-energy particle precipitation to the upper atmosphere (Knipp et al., 2013) and depletion of relativistic electrons fluxes in the outer Van Allen radiation belts (e.g., Hietala et al., 2014; Turner et al., 2019) can occur due to the sheath passage.

The importance of ICME sheaths to space weather results from their high dynamic pressure and southward magnetic fields (see e.g., Boudouridis et al., 2005; Burton et al., 1975; Crooker, 2000; Kilpua et al., 2019; Lindsay et al., 1995). The key mechanisms generating southward fields in the sheath are shock compression of pre-existing out-of-ecliptic fields in the solar wind, turbulence downstream of an interplanetary shock, and field line draping of the interplanetary magnetic field (IMF) around the driving ejecta (Lugaz et al., 2016; Tsurutani et al., 1988). Improved space weather predictions require a comprehensive understanding of the interplay between the ICME and the Earth's magnetosphere, and the ability to determine these southward fields within the ICME sheaths (Tsurutani et al., 2020). Moreover, spatial variability of sheath fields in the longitudinal direction at 1 AU and its consequences for space weather has been addressed by Ala-Lahti et al. (2020). The ICME sheath fields have a large-scale structure being more coherently structured compared to the solar wind. They, however, also host local and spatially limited magnetic fluctuations, the space weather impact being thus dependent on the magnetic fine structure of the ICME sheath (see also Good et al., 2020). Discrete magnetic field discontinuities embedded in an ICME sheath can cause abrupt compression of the dayside magnetosphere and excite wave generation in the inner magnetosphere (Blum et al., 2021).

Direct observations of the interaction between an ICME sheath and the Earth's magnetosphere, including the transmission of an ICME sheath into the Earth's magnetosheath, are important for constructing a thorough picture of the interaction. A dominant process for geomagnetic disturbances is dayside magnetic reconnection requiring a southward field in the magnetosheath. This is typically from the southward IMF but can also be locally southward from magnetosheath transients such as high speed jets (Nykyri et al., 2019). Therefore, we need a complete understanding of how the various structures inside the ICME sheath interact with the dayside magnetosphere since they can possibly dictate the field direction at the dayside magnetopause.

In this study, we examine the sheath region of the ICME on 13 May 2005. The ICME and its impact on the Earth's magnetosheath have been previously studied (e.g., Bisi et al., 2010; Dasso et al., 2009; Turc et al., 2014; Yurchyshyn et al., 2006). The impact of the ICME ejecta on the Earth's magnetosheath has also been investigated statistically (Turc et al., 2017). The ICME-driven sheath region was observed at 1 AU on 15 May 2005, first by the ACE and Wind spacecraft in the upstream solar wind, subsequently by the Cluster spacecraft, and finally by the Geotail spacecraft in the Earth's magnetosheath. We investigate the occurrence of magnetic structures and fluctuations embedded in the ICME sheath that were transmitted, across the Earth's bow shock and into the magnetosheath. With transmit we refer to magnetic field features and properties in the bow shock downstream region, which were observable already in the upstream. We also examine if the upstream magnetic field fluctuation frequency affects how well the structures maintain their characteristics across the shock. The location of Cluster, in the immediate upstream of the bow shock during the event, constitutes the frame of reference in this study. We focus on the southward component of the transmitted structures, while considering the overall dynamics of the bow shock during the ICME sheath-magnetosheath encounter.

The study is constructed as follows. Section 2 introduces the range of spacecraft observations during the ICME event at 1 AU on 15 May 2005. Section 3 focuses on the magnetic field within the ICME sheath that is transmitted to the Earth's magnetosphere, and the spatial and temporal extent of the identified magnetic structures. Section 4 discusses the relation of the observations to bow shock dynamics. Section 5 concludes with discussion.

2. Observations

Magnetic field data with a resolution of 10.9 Hz from Wind (Lepping et al., 1995), 1 Hz from ACE (Smith et al., 1998), 22.4 Hz from Cluster (Balogh et al., 1997), and 16 Hz from Geotail (Kokubun et al., 1994) are analyzed in this study. We also present and analyze data from the Wind Solar Wind Experiment (Ogilvie et al., 1995), from the ACE Solar Wind Electron Proton Alpha Monitor (SWEPAM; McComas et al., 1998), from the Cluster Ion Spectrometry (CIS) Experiment (Réme et al., 1997), and from the Geotail Low Energy Particle (LEP) Experiment (Mukai et al., 1994).

Figures 1a–1c show the spacecraft locations and the global ICME observations at 1 AU on 15 May 2005 in Geocentric Solar Ecliptic (GSE) coordinates. The panels present a sketch of the magnetopause (black) and bow shock (red) boundaries during the sheath passage, with the trajectories of the Cluster 3 and Geotail spacecraft shown for 01:00–06:00 UT and Figure 1c having a cut-out of the GSE x-axis. ACE and Wind, both in the proximity of L1, had a relatively large longitudinal separation during the event, ACE being close to the Sun-Earth line and

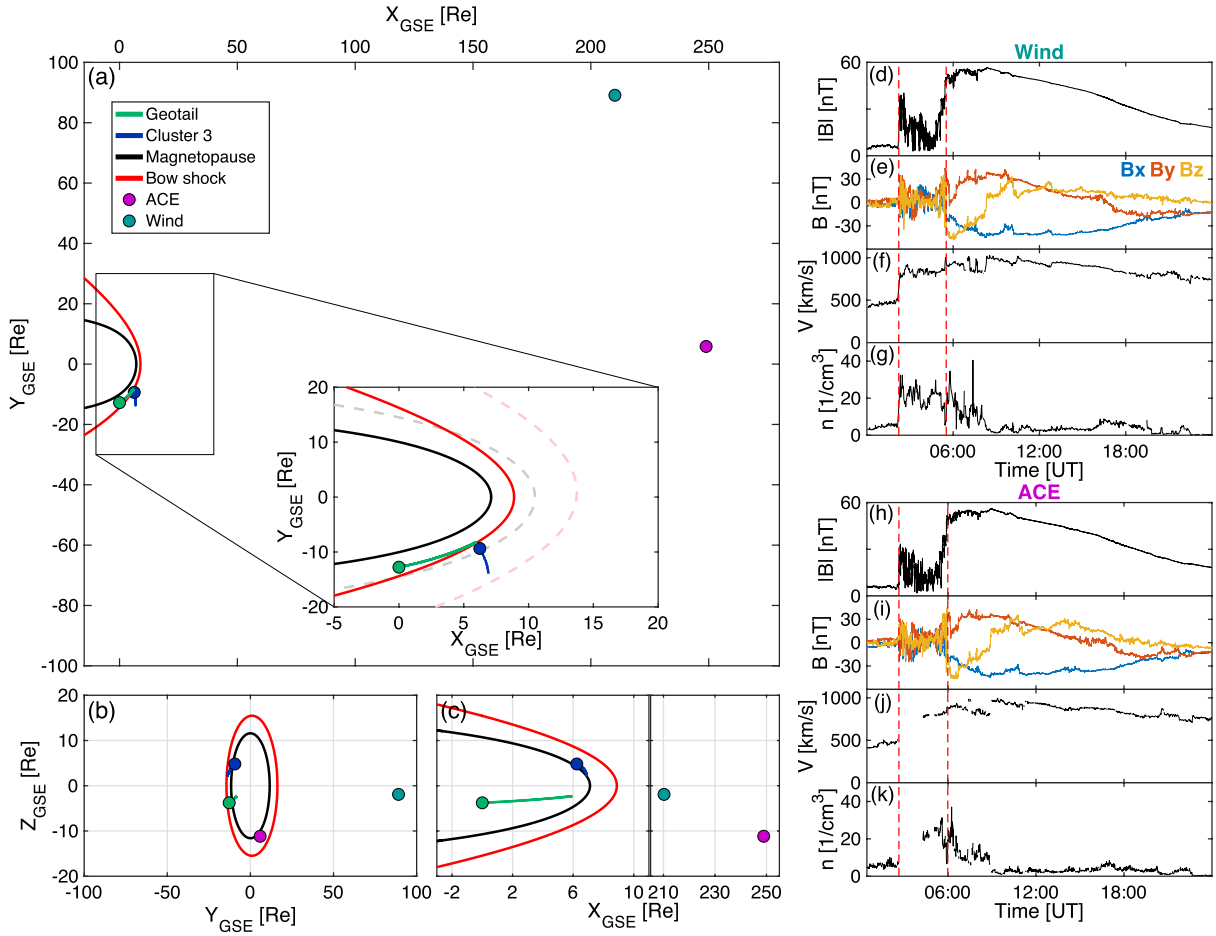

Figure 1. (a–c) Sketch of near-Earth space in Geocentric Solar Ecliptic (GSE) coordinates at 01:00–06:00 UT on 15 May 2005 showing the trajectories of the Geotail (green) and Cluster 3 (blue) spacecraft, and the mean positions of the ACE (purple) and Wind (teal) spacecraft. The change in position for ACE and Wind was negligible in this time period, unlike for Geotail and Cluster 3. Earth's magnetopause (solid black lines) and bow shock (solid red lines) are modeled during the interplanetary coronal mass ejection (ICME) sheath passage using Wind measurements (Merka et al., 2005; Shue et al., 1998). Dashed lines in panel (a) indicate the magnetosheath boundaries for the solar wind conditions prior to the ICME arrival. There is a cut-out of the GSE *x*-axis in panel (c). (d–g) Magnetic field magnitude (|B|), magnetic field components (B), speed (*V*), and proton density (*n*) measured by Wind and (h–k) ACE on 15 May 2005. Vertical red dashed lines indicate the times of the interplanetary shock preceding the ICME sheath (ACE 02:11 UT; Wind: 02:13 UT) and the leading edge of the driving ICME (ACE: 05:30 UT; Wind: 05:31 UT).

Wind at about 90 R_E duskward. The change in location of ACE and Wind during the observation time period was negligible. The GSE *y*-separation between ACE and Cluster 3 (Geotail) was between 15 and 20 R_E (14–19 R_E). Between Wind and Cluster 3 (Geotail), the separation varied from 98 to 103 R_E (from 97 to 102 R_E). The insert in Figure 1a also illustrates the magnetosheath boundaries during nominal solar wind conditions preceding the ICME (dashed curves). It can be seen that the ICME sheath compressed the magnetosheath resulting in the Cluster 3 spacecraft entering from the magnetosheath into the bow shock upstream region. Geotail was located in the magnetosheath flank during the entire ICME sheath passage apart from short visits in the bow shock upstream region between ~05:13–05:15 UT and ~05:36–05:41 UT, initially quite far downstream from the point where Cluster 3 exited the magnetosheath. In this study, "upstream" refers to Cluster 3 observing the ICME sheath prior to its interaction with the bow shock and magnetosheath, and "downstream" refers to the Geotail observations in the magnetosheath during the ICME passage. Geotail traveled toward the bow shock during the event and the separation with Cluster decreased during the course of the event.

Figures 1d–1g and 1h–1k show the magnetic field (B), plasma speed (*V*) and proton density (*n*) measurements from ACE and Wind during the event. The ICME sheath is bounded by the red vertical lines. ACE and Wind observed the interplanetary shock at 02:11 and 02:13 UT, and the ejecta leading edge at 05:30 and 05:31 UT, respectively. The measurements display strong fluctuations of both magnetic field magnitude and its components,

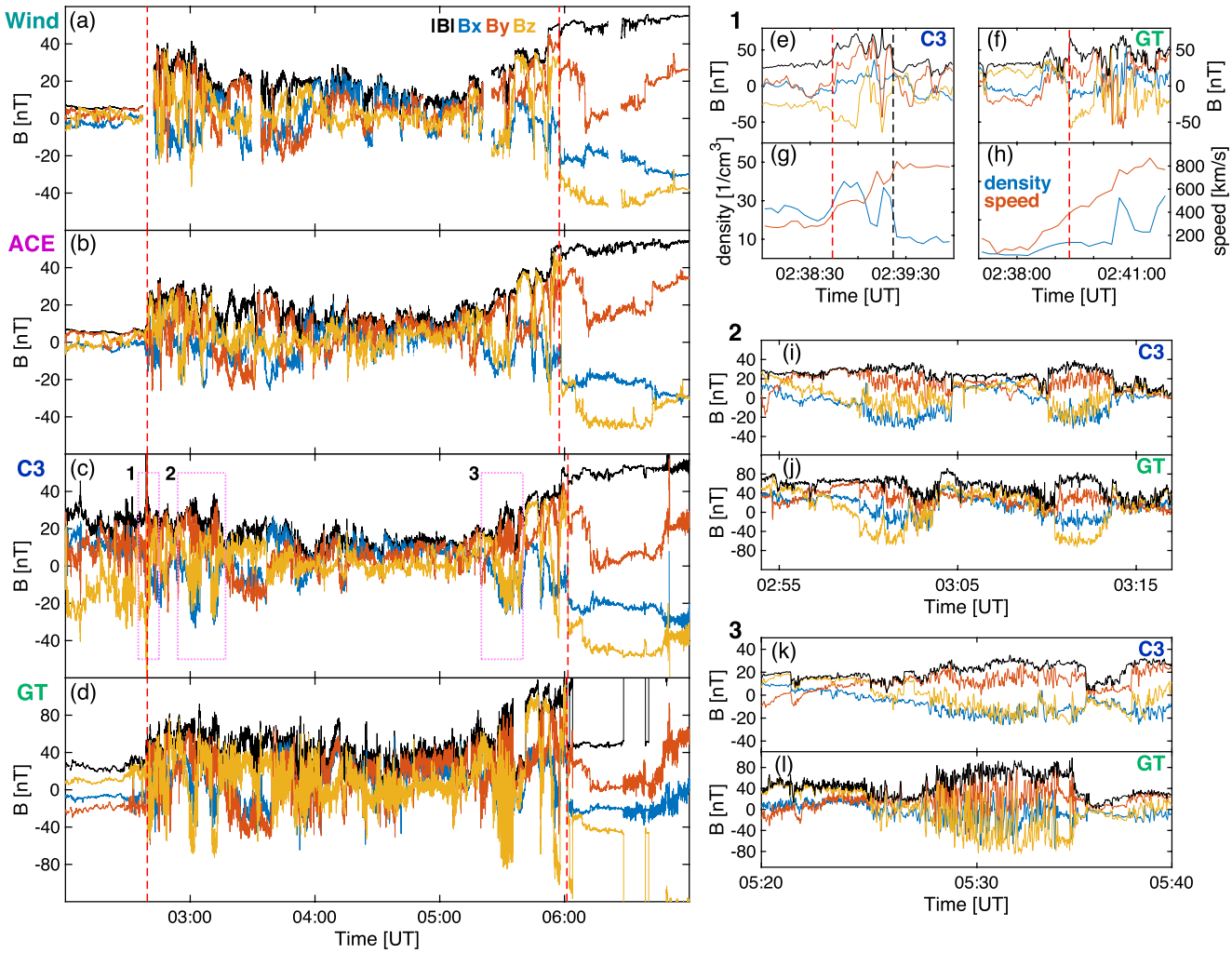

Figure 2. (a–d) Magnetic field measurements from Wind, ACE, Cluster 3 (C3) and Geotail (GT) during the ICME-driven sheath region on 15 May 2005, at 1 Hz resolution. The measurements are time-shifted and aligned relative to the beginning of the event at C3 (dashed red lines). The pink boxes in panel (c) indicate three intervals of interest, as follows: (1) the beginning and arrival of the interplanetary coronal mass ejection (ICME) sheath indicated by a fast forward interplanetary shock, and (2 and 3) substructures in the C3 data, which have a notable negative out-of-ecliptic component and that also appear in the Geotail data. The dashed red lines at ~06:00 UT indicate the trailing edge of the sheath that is, the leading edge of the driving ICME ejecta. Selected data from the three intervals are shown in panels (e–l). The magnetosheath exit of C3 is marked by the black dashed line. Proton density and plasma speed are shown for the interval 1 in panels (g–h).

and significant variations in plasma parameters, all characteristic features of an ICME sheath region (e.g., Kilpua, Koskinen, & Pulkkinen, 2017). The driving ICME ejecta is clearly noticeable from the smooth rotating magnetic field.

Figure 2 focuses on magnetic field measurements during the ICME sheath crossing. We have resampled the magnetic field data to 1 Hz resolution, the highest resolution available for all four spacecraft. Panels (a–d) are sorted according to the GSE *y*-component of the spacecraft position at the beginning of the event, with Wind measurements at the top and Geotail (GT) measurements at the bottom. The measurements are time-shifted so that the arrival time of the ICME sheath, marked by the red dashed vertical line, coincides at all spacecraft. The arrival time at Cluster 3 (C3), 02:38:45 UT on 15 May 2005, is used as the reference time, the used time-shifts being 25 min 45 s, 27 min 35 s, and −20 s, for Wind, ACE, and GT, respectively. Upon inspecting the simultaneous ICME sheath and magnetosheath observations, there are common structures observed in both datasets with remarkable similarities. The goal of the study is to understand the physical nature of how these magnetosheath structures arise. Three intervals of interest labeled 1–3 are highlighted with pink dotted rectangles in Figure 2c. Selected data from these intervals are shown at smaller scales in the right-hand panels in Figures 2e–2l, with corresponding labels 1–3 and interval 1 augmented with plasma observations in Figures 2g and 2h.

At C3, interval 1 spans the arrival of the ICME and the exit of the spacecraft from the Earth's magnetosheath. In Figure 2c, it can be seen in interval 1 that there were fluctuations with relatively large amplitude and similar magnetic field magnitudes (|B|) before and after the sheath arrival time. C3 was in the magnetosheath before the ICME encountered the magnetosphere, as indicated by the |B| values of 25–30 nT and proton densities of ∼25 cm^{-3} before the arrival of the sheath, which are much higher values than those observed in the solar wind before the sheath arrival at L1. The sheath arrival at C3 is manifested by the enhancement of the magnetic field magnitude and increases of n and V. The plasma speed gradually increased until C3 exited the magnetosheath at 02:39:22 UT, the exit being also indicated by a drop in |B| and n. The C3 magnetosheath exit is marked by the black dashed vertical line in the interval 1 in Figures 2e and 2g. Data from the equivalent interval at GT show that the beginning of the event is defined by an abrupt increase of |B|.

Three intervals with notable southward field components can be distinguished with visual inspection of the C3 measurements in Figure 2c. They are also distinct at GT and occur in the same chronological order at both spacecraft, suggesting that at least part of their properties were preserved as they transmitted from the upstream into the magnetosheath. These intervals are marked by the second and third rectangles (i.e., intervals 2 and 3) in Figure 2c and are highlighted in the corresponding right-hand panels in Figures 2i–2l. The C3 and GT spacecraft made these observations with longitudinal separations of 0.3 R_E and 4.8 R_E, respectively. During these three intervals the magnetic field fluctuated substantially, and the out-of-ecliptic component, B_z, in the upstream at C3 had average values of −4.8, −9.1, and −11.8 nT, in chronological order. The average was 5.3 nT elsewhere in the sheath. Corresponding B_z values in the magnetosheath at GT during the ICME sheath passage were −16.8, −38.0, and −34.8, and 14.0 nT, respectively. The values of |B| were also enhanced during these intervals (C3: 28.2, 29.9, and 26.0, and 17.7 nT; GT: 58.2, 58.0, and 63.2, and 43.4 nT). We will investigate these intervals in more detail below.

In addition, all spacecraft observed prominent large-scale field variations at the back of the ICME sheath, the boundary between the ICME sheath and ejecta being marked by red dashed lines at ∼06:00 UT. The duration of the sheath passage is slightly longer at C3 and GT than at Wind and ACE.

3. Correlation Analysis

We compute the Pearson correlation coefficients for the magnetic field measurements in the intervals that, according to the previous visual investigation, were transmitted to the Earth's magnetosphere during the ICME sheath passage on 15 May 2005. We also investigate how the transmission of ICME sheath magnetic fields may depend on the frequency of the field fluctuations, and whether the transmitted field features were long-lasting occurrences in the ICME sheath prior to encountering the magnetosphere. The first 37 s of the ICME sheath interval at C3, when the spacecraft was still within the magnetosheath, are excluded from the analysis by marking the ICME sheath beginning at C3 at 02:39:22 UT (see the black dashed vertical line in Figure 2e).

Similar to Ala-Lahti et al. (2020), we compute the total Pearson correlation by applying the averaging estimator of correlation coefficients (Olkin & Pratt, 1958) for the individual Pearson correlation coefficients of the magnetic field magnitude and components. Pearson correlation coefficient measures the linear dependence of two random variables and is used to compare spacecraft measurements (e.g., Good et al., 2018; Lugaz et al., 2018). The overall or total correlation is defined as

$$\sigma_{tot} = \frac{\sum_{i=1}^{4}(n_i - 1)}{\sum_{i=1}^{4}(n_i - 4)} \left[\sigma_{P,i} + \frac{\sigma_{P,i}(1 - \sigma_{P,i}^2)}{2(n_i - 3)}\right], \quad (1)$$

where i refers to the magnetic field magnitude or component, $\sigma_{P,i}$ is the corresponding Pearson correlation coefficient, and n is the size of the sample (Ala-Lahti et al., 2020; Alexander, 1990).

We compute σ_{tot} for the C3 and GT data for the identified three intervals in order to quantify the visual similarity at the two spacecraft. We select the intervals in the upstream (C3) as follows: (1) 02:59:29–03:04:39 UT, (2) 03:10:03–03:13:49 UT, and (3) 05:28:09–05:35:49; and hereafter, refer to these intervals as “structures” in the magnetic field. The boundaries are based on a number of features in the magnetic field observations in the upstream, such as abrupt changes in the magnitude or orientation of the magnetic field, or the onset or ending of significant fluctuations. All the structures were convected by the bulk flow, checked by performing the timing analysis (Eastwood, Balogh, et al., 2005; Paschmann & Daly, 1998) using data from all four Cluster spacecraft.

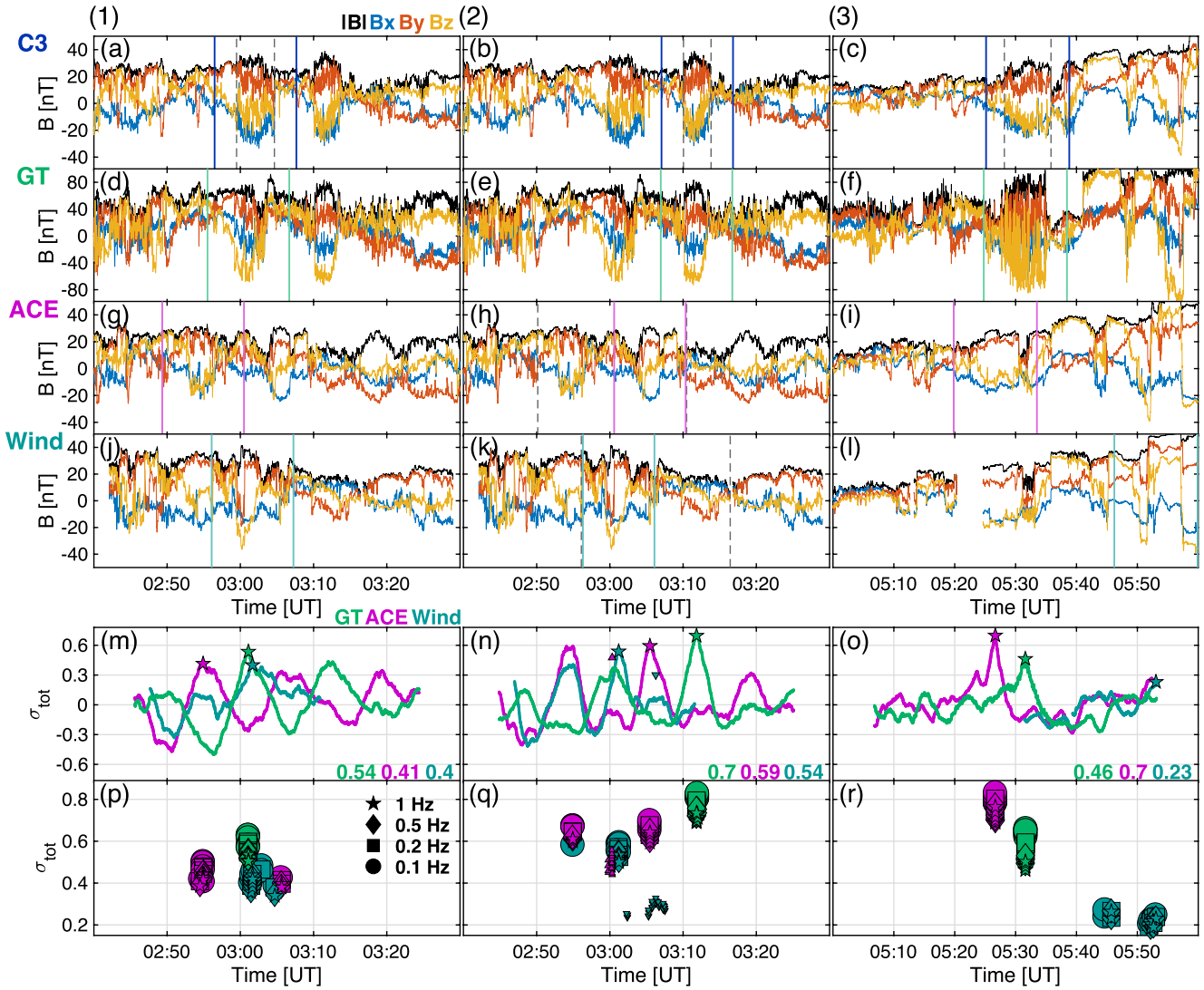

Figure 3. Correlation coefficient analysis comparing the correspondence of Geotail, ACE and Wind magnetic field data to a sub-interval of C3 data defined by boundaries marked with blue vertical lines in panels (a–c). Columns 1–3 correspond to structures (1–3), respectively. (a–l) The magnetic field data of the spacecraft. (m–o) The total cross-correlation (σ_{tot}) of the subinterval given in panels (a–c) with the data at the other spacecraft. Correlation values were calculated for sub-intervals at the other spacecraft with durations equal to that of the corresponding C3 interval. Correlation values at the mid-point of the sliding intervals are shown in panels (m–o). Peak values in the cross-correlation are indicated by stars and corresponding numerical values given in the bottom right corners of panels (m–o). Panels (p–r) show how the location of these highest correlations vary when the boundaries marked by the blue vertical lines in panels (a–c) vary and when data are resampled to lower resolutions (to 0.5, 0.2, and 0.1 Hz). The boundaries in panels (a–c) are the identified structure boundaries with 3 min added before and after. These additions in panels (p–r) vary from 1:30 min to 4:30 min in steps of 30 s, the addition of 3 min representing the middle value of this vector. The gray dashed lines in panels (h) and (k) indicate the intervals corresponding the peak values marked by an upward and downward pointing triangles in panel (n), when structures (1) and (2) are considered together at ACE and Wind, respectively. The triangles in panel (q) show how the location of these highest correlations vary when the data resolution and interval length are varied.

In order to have well-defined correlation coefficients that account for distinguishable features of the structures, we have to consider longer intervals than the ones defined by the three structures. We note that the definitions of the structure boundaries include some degree of subjectivity. We control this subjectivity by varying the duration of the structure intervals when computing σ_{tot}. Furthermore, we examine the characteristics of the structures at L1 (ACE and Wind).

Figures 3a–3c show C3 data, with the structure boundaries marked by gray dashed vertical lines. Panels (d–l) show GT, ACE, and Wind data. The magnetic field data shown in each plot are aligned relative to the beginning of the sheath arrival at C3 (02:39:22 UT shown in Figure 2). The spacecraft data is resampled to 1 Hz.

The intervals bounded by the blue solid vertical lines in Figures 3a–3c demarcate intervals ±3 min of the structure boundaries. These extended C3 intervals are cross-correlated with the data at GT, ACE, and Wind shown in Figures 3d–3l, with σ_{tot} calculated at each step of the cross-correlation. The resulting series of σ_{tot} values are given in Figures 3m–3o. The σ_{tot} time series show the correlation at each time step, with the investigated GT, ACE, or Wind intervals being centered at the time step. The maxima of the σ_{tot} cross-correlations are indicated by stars for each series, with the maxima values listed at the bottom right corners of the panels. Pale solid vertical lines in Figures 3d–3l indicate the data intervals that give the maxima in σ_{tot}. The analysis is defective for structure (3) at Wind because of a data gap.

In addition to the extended ±3 min intervals, we repeat the above analysis by considering the structures with ±1.5–4.5 min extensions in steps of 30 s. We also consider the spacecraft data resampled to 0.5, 0.2, and 0.1 Hz. Figures 3p–3r show the locations of maximum correlation, similar to the stars in Figures 3m–3o. Different markers indicate the resampling resolution used but they do not distinguish different interval lengths used in our analysis.

The correlation analysis presented in Figure 3 suggests that the structures in the upstream, that is, in the C3 data, were transmitted to the magnetosheath and observed by GT. The intervals identified by the correlation analysis, marked by the pairs of pale vertical lines in Figures 3d–3f, coincide with the previous visual inspection of the data. Furthermore, the analysis presented in Figures 3p–3r indicates that the identification is robust: The position of maximum correlation does not depend on the resampling resolution or on the precise length of the interval centered on the structure. This is indicated by the stable position of the green markers, and it applies for all three upstream structures. We note that as the duration of the structure remains much greater than the resampling resolutions, the σ_{tot} values increase as resampling resolution decreases due to the lower resampling resolution smoothing out the high frequency fluctuations observed within the structures.

The comparison of structures (1) and (2) at C3 with the observations at ACE and Wind gives lower σ_{tot} maxima than with GT (Figures 3g–3f, 3j–3k, and 3m–3n), which may result from the spacecraft at L1 having a different cross-section through the structures. The times giving maximum σ_{tot} also vary depending on the resampling resolution and interval length used (Figures 3p and 3q). Moreover, the same interval at Wind is identified as the most probable candidate for both structures (1) and (2) in the correlation analysis. The same appears also for ACE to some extent, when considering Figures 3m–3n and 3p–3q. Visual inspection on the other hand suggests that the intervals centered at ∼02:55 UT at ACE and at Wind correspond to each other in Figures 3g and 3j. The intervals marked by the vertical lines in Figures 3h and 3k also exhibit visual similarity.

The occurrence of structures (1) and (2) at L1 is further investigated by studying them together. Similar to the analysis above, an interval bounded by the beginning of structure (1) (the first gray dashed line in Figure 3a) and the ending of structure (2) (the second gray dashed line Figure 3b) is compared to the ACE and Wind data. The intervals giving the maximum correlations are marked by the gray solid lines in Figures 3h and 3k, and the corresponding σ_{tot} values given by the upward and downward pointing triangles for ACE and Wind in Figure 3n, respectively. The purple triangles in Figure 3q, which do not differentiate different resampling resolutions, indicate a robust identification at ACE. The teal triangles for the comparison with the Wind data are more scattered and indicate relatively small correlation.

This is consistent with the findings reported by Ala-Lahti et al. (2020), namely that magnetic fluctuations in ICME sheaths exhibit spatial structuring with heliospheric longitude at 1 AU. This can explain the ambiguity in identifying structures (1) and (2) at L1, especially at Wind, which had a relatively large longitudinal spacecraft separation with C3 during the observation time period (Section 2 and Figures 1a–1c). However, the combined identification of structures (1) and (2) at ACE implies the structures had a larger than 15 R_E longitudinal width, a conclusion not possible from the comparison of the data from C3 and GT. In addition, some structures evidently are large-scale and spatially coherent across the ICME sheath and sufficiently long-lasting, such as structure (3), which is robustly identified by the correlation analysis at ACE and by eye at both ACE and Wind (see Figure 3), and the prominent large-scale field variations at the back of the ICME sheath.

Alternatively, the magnetic fields of an ICME sheath may develop substantially while traveling from L1 to the Earth. Consequently, observations at L1 would not always be sufficient to forecast, for example, strong southward magnetic fields in the Earth's magnetosheath, such as those seen in structures (1) and (2).

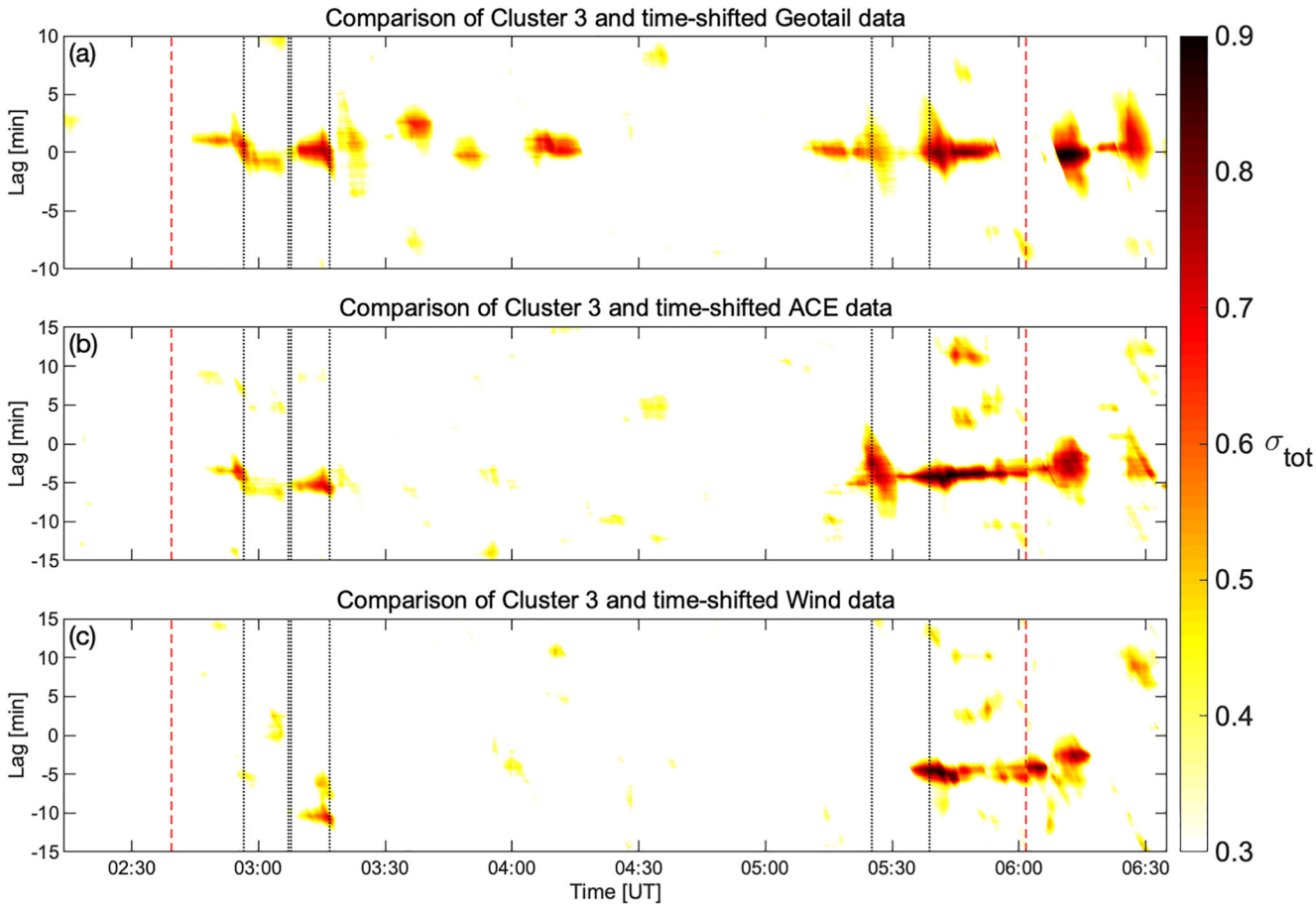

Figure 4. Total correlation between the magnetic field measurements at C3 and the other spacecraft. (a–c) σ_{tot} for C3 data correlated with time-shifted Geotail (GT), ACE, and Wind data, respectively. Red vertical dashed lines indicate the shock and interplanetary coronal mass ejection (ICME) leading edge, and black dotted lines are the boundaries given in Figure 3a. Subintervals of C3 and GT data are compared to each other by taking a 10 min subinterval of C3 data and the 20 min surrounding of corresponding (time-shifted) GT/ACE/Wind data. A subinterval of C3 data, of which the observation time is given on the horizontal axis, is compared to a corresponding sub-interval of GT/ACE/Wind data, the values of σ_{tot} being computed by shifting the location of this subinterval of GT/ACE/Wind data. The shift is defined as the lag. The lower boundary of the color bar, $\sigma_{tot} = 0.30$, is the lower quartile of the distribution of correlation maxima defined in the text.

We extend the above analysis for the whole ICME sheath on 15 May 2005 to examine how the identified structures compare to other magnetic field features during the event. We compare 10 min C3 intervals resampled at 1 Hz to intervals at GT. A 10 min interval is comparable in duration to the intervals indicated by the blue vertical lines in Figure 3. Again, the spacecraft measurements are aligned using the sheath arrival time as reference, and we compare a C3 interval to a set of GT intervals similarly as in Figure 3. The results for the cross-correlation of the C3 intervals with the time-shifted GT data are shown in Figure 4a, where the time on the horizontal axis gives the center of the C3 interval in question, and where the lag on the vertical axis gives the difference in time between the centers of the C3 and GT intervals analyzed. The red dashed lines indicate the beginning and end of the ICME sheath event and the black dotted lines indicate the intervals given by the blue lines in Figure 3. The corresponding analysis for time-shifted ACE and Wind is shown in Figures 4b and 4c, respectively.

Consistent with our previous results, Figure 4a highlights structures (1–3) (bounded by the black dotted lines) and their surroundings with relatively higher values of σ_{tot}. In addition, the map suggests that the structures were not sole "survivors" in the transmission of the ICME sheath to the Earth's magnetosheath. The map distinguishes patches of relatively high correlation between ~03:20 and 04:20 UT. These correspondences in the field features in the upstream (C3) and downstream (Geotail) are also evident from visual inspection of the timeseries (see Figures 2c and 2d). During the period at ~03:25–03:37 UT, B_z was positive and B_x and B_y negative, with the interval ending at a sharp polarity reversal of the magnetic field direction. During ~04:05–04:15 UT, the field components experienced a polarity reversal, B_z (B_x and B_y) being at first negative (positive). The magnetic field

in the upstream additionally experienced a gradual rotation at ~03:46–03:52 UT, which is not observable by eye in Figure 2 but which appears in Figure 4a as a patch of high correlation. We note that, contrary to the structures (1–3), the intervals discussed here do not have noteworthy southward B_z (see Figures 2c and 2d).

In particular, structures (2) and (3) are discernible in terms of patches that indicate a considerable correlation in Figure 4b for ACE. The same applies for structure (1) to some extent. Figure 4c for Wind shows only weak associations for structures (1) and (2), but there is a period of high correlation at the back of the sheath at both spacecraft. The better correlations with ACE can depend on the GSE y location of the spacecraft (see Figure 1). This implies spatial variability in ICME sheaths, with the spacecraft location being sensitive to detecting different features in the magnetic fields. The back of the ICME sheath after structure (3) exhibits a well-correlated period at all spacecraft, corresponding to visually discernible large-scale field variations. The panels do not display significant patches elsewhere in the ICME sheath. These observations are in agreement with our analysis in Figures 2 and 3.

We complete our correlation analysis by examining the dependence of the transmission of upstream ICME sheath magnetic fields into the Earth's magnetosheath on the frequency of the field fluctuations. First, we define two thresholds for σ_{tot}. We construct a distribution of σ_{tot} values by taking the maximum value at each point in time during the ICME sheath passage in Figure 4a, that is, the maximum correlation across the lag range at each time. The median and upper quartiles of the resulting σ_{tot} distribution are 0.48 and 0.60. The lower quartile of the distribution is $\sigma_{tot} \simeq 0.30$ and set as the lower limit of the color bars in Figure 4. Next, we band-pass filter the C3 and GT magnetic field data, compute σ_{tot} values similar to those in Figure 3, construct the distribution of the maximum correlations and compute the percentage of the distribution above the thresholds defined above. We examine 10 bands with frequency ranges defined by $\beta \cdot 10^{\alpha}$ Hz, where β is equal to 1.0–2.5, 2.5–5.0, 5.0–7.5, and 7.5–10.0 Hz, and α varies from -3 to -1; the two highest β ranges are excluded when $\alpha = -1$, giving 10 bands in total. We also vary the length of the investigated intervals from the 10 min used earlier, computing in addition σ_{tot} for 5, 20, and 30 min C3 data intervals.

The patches in Figure 5a coincide with the intervals identified and discussed previously; within a given patch, the color denotes the highest frequency range for which there is good correlation (i.e., $\sigma_{tot} \geq UQ$). In addition, the highest frequency band given in the figure shows multiple patches with different lags for a given time. This may result from wave-like features prevailing in the frequency band, with waves having a different phase between the locations in upstream and downstream where the observations were made. The analysis for all frequency bands, interval lengths and both correlation thresholds is summarized in Figure 5b, which shows the percentage of the band-pass-filtered σ_{tot} distribution above a given threshold (0.48 or 0.60) as a function of frequency. The legend indicates whether only 10 min or all data interval lengths are considered. In the latter case, the average of percentages across the four different interval lengths is computed. Additionally, the legend indicates the threshold used (given in brackets). The horizontal error bars in the figure show the frequency bands for other than the highest frequencies where they would overlap.

Figure 5b gives an indication of the frequency dependence of the transmission of magnetic fluctuations from the ICME sheath into the Earth's magnetosheath. We note our analysis is limited, for example, due to changes in spacecraft position and a relative large spacecraft separation that restrict the subsequent observations of short-lived small-scale fluctuations. However, larger-scale fluctuations in ICME sheath exhibit less spatial variability (Ala-Lahti et al., 2020) and the results presented in Figure 5 are an indicative of a trend. The figure shows that the probability of feature transmission increases significantly for frequencies below ~0.01 Hz. This finding is in agreement with Rakhmanova et al. (2015), who reported similar frequency ranges when examining solar wind origin magnetic fluctuations in the Earth's magnetosheath. They concluded that bow shock and magnetosheath processes contribute considerably to the distribution of magnetic fluctuations at higher frequencies. Furthermore, they suggested that higher-frequency magnetic fluctuations might also enter the magnetosheath if embedded in dense solar wind with large |B|. ICME sheaths are solar wind transients which typically exhibit both of these conditions (e.g., Kilpua, Koskinen, & Pulkkinen, 2017). However, the increase in probability in Figure 5 occurs only at frequencies below ~0.01 Hz, possibly due to the limitations noted above. We further discuss the transmission of higher-frequency fluctuations in the next section, because waves at higher frequencies in the upstream are thought to transmit to the downstream (e.g., Clausen et al., 2009; Francia et al., 2012; Takahashi et al., 2021; Villante et al., 2011).

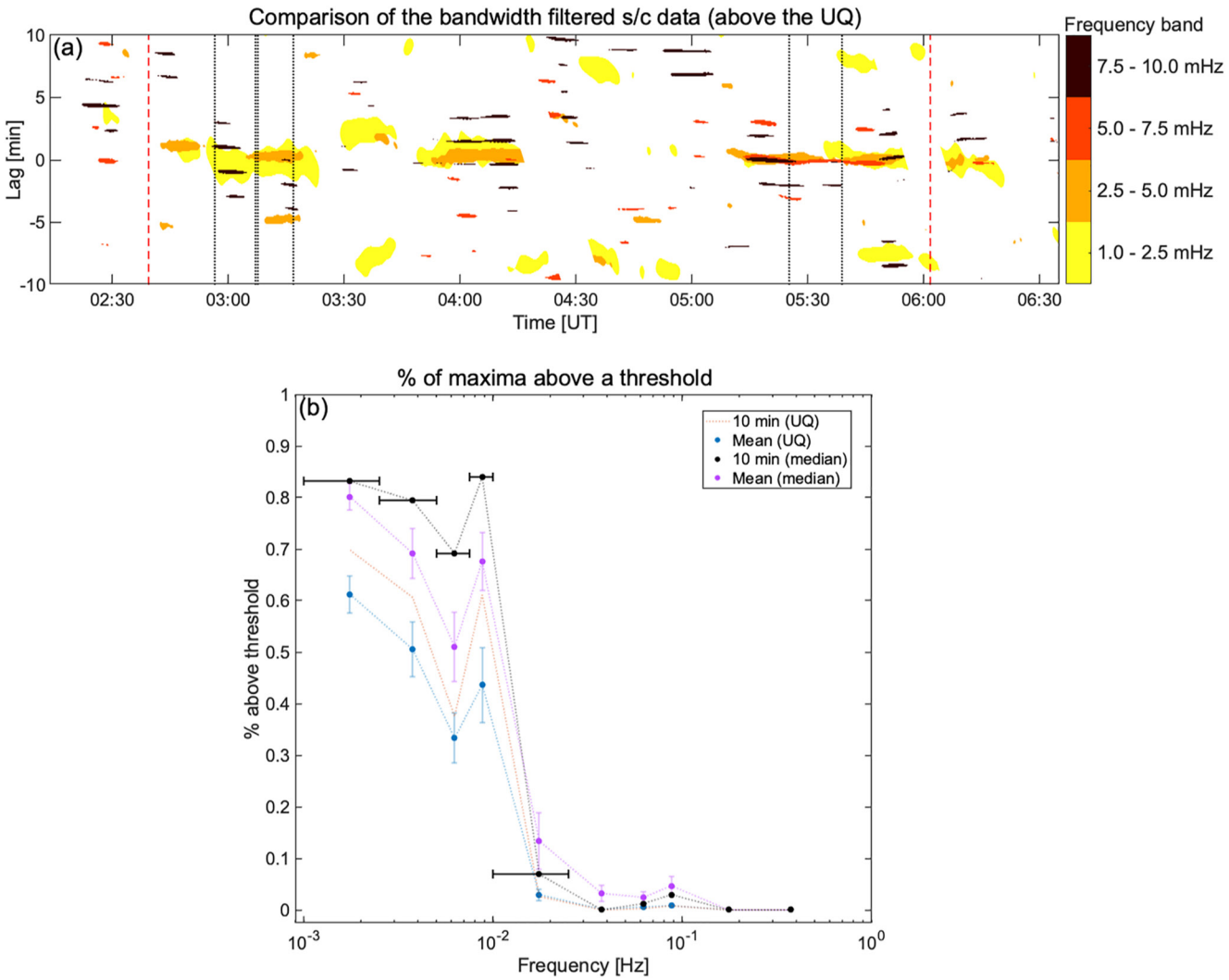

Figure 5. (a) Total correlation between the band-pass-filtered magnetic field data at C3 and GT during the interplanetary coronal mass ejection (ICME) passage. Patches in the map show when the threshold of $\sigma_{tot} = 0.60$ is exceeded, and colors indicate the frequency bands investigated. The threshold is the upper quartile (UQ) of the distribution of correlation maxima defined in the text. (b) The percentage of σ_{tot} maxima as a function of bandwidth filtered spacecraft data. The percentages are computed for different interval lengths and different thresholds. The percentages are shown when 10 min C3 intervals were considered, and when the average of 5, 10, 20, and 30 min intervals were computed. The vertical error bars give the standard error of the mean. The thresholds are the median ($\sigma_{tot} = 0.48$) and UQ ($\sigma_{tot} = 0.60$) of the distribution of correlation maxima defined in the text. The black horizontal bars indicate the frequency bands used. The trend of the bands is also applied for the highest frequency bands but not shown due to all curves overlapping. "*s/c*" refers to spacecraft.

We conclude that magnetic structures (1–3) embedded in the ICME sheath observed on 15 May 2005 were transmitted into the Earth's magnetosheath. They are detectable in the spacecraft data by visual inspection and stand out in our correlation analysis. The structures differed from other discernible intervals in the correlation analysis due to their southward field components, which were notably amplified when transmitted into the Earth's magnetosheath. There is, however, ambiguity as to whether these structures were present further upstream at L1. Not all fluctuations appearing in the upstream did survive the transmission into the downstream, only lower-frequency fluctuations transmitting into the magnetosheath.

4. Bow Shock Dynamics: Traveling Foreshocks

We here continue the examination of structures (1–3) by relating them to the bow shock dynamics. We have estimated the bow shock angle, defined as the angle between the shock normal and upstream magnetic field direction (θ_{Bn}), by following the field lines given by the C3 measurements during the ICME sheath passage and by

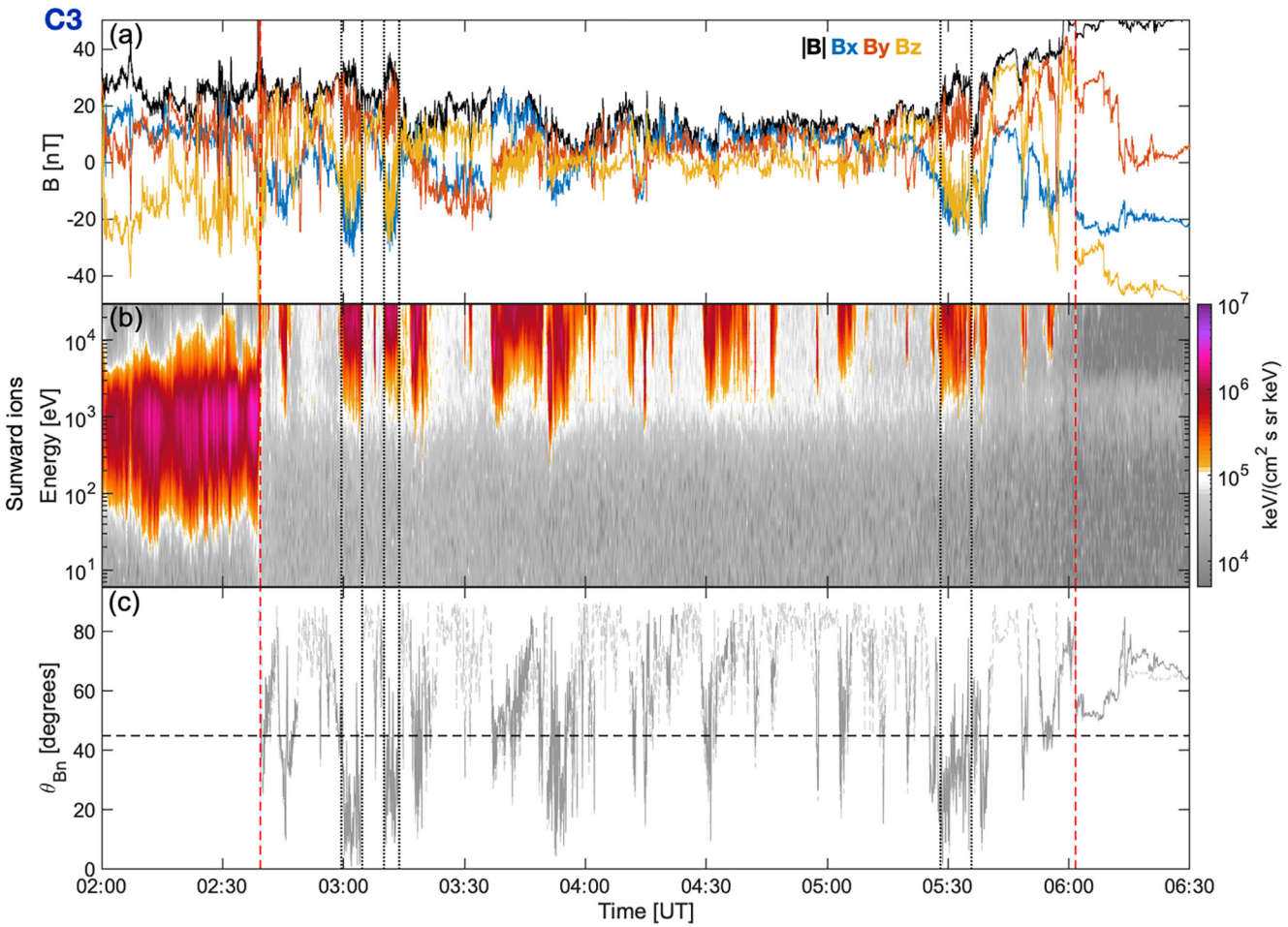

Figure 6. (a) C3 magnetic field measurements and (b) corresponding energy flux of sunward-traveling ions. (c) The estimated shock angle (θ_{bn}) of the Earth's bow shock when the magnetic field at C3 (solid gray) is extrapolated to the bow shock configuration according to Merka et al. (2005). The dashed gray curve indicates θ_{bn} when the path along the magnetic field direction given by C3 observations does not cross the bow shock due to the orientation of the magnetic field, and the radial path from the location of C3 to the center of the Earth is used instead. Black dotted vertical lines indicate the structure boundaries given in Figure 3a.

modeling the bow shock using the model by Merka et al. (2005). This estimation is compared to the particle energy flux of the sunward traveling ions measured by the C3 CIS instrument. The C3 measurements and estimated bow shock angle during the event are presented in Figure 6, where black dotted vertical lines mark the structure boundaries. In Figure 6c, which shows the bow shock angle θ_{Bn}, the solid gray curve gives the angle along the upstream field lines while the dashed one gives the estimation during periods when the field lines did not connect to the bow shock, the angle being then estimated along the straight radial path from the spacecraft to the Earth.

Figure 6 indicates that, during the event, C3 frequently observed fluxes of sunward traveling ions, which correspond to ions reflected from the bow shock, and which are an observational characteristic of a foreshock upstream of the bow shock (e.g., Eastwood, Lucek, et al., 2005). The observed sunward fluxes were coincident with the upstream magnetic field lines encountering the bow shock, as demonstrated by the solid gray curve. Sunward traveling (or backstreaming) ions have been previously observed for $\theta_{Bn} \leq 70°$ (e.g., Eastwood, Lucek, et al., 2005). Moreover, the shock angle varied considerably and rapidly during the sheath passage. During the structures identified in this study, the bow shock was quasi-parallel ($\theta_{Bn} < 45°$), the structure boundaries being associated with abrupt changes of θ_{Bn}. Fluxes of backstreaming ions were additionally observed during all three structures, which suggests that the structures constituted transient foreshocks. With a transient foreshock we refer to a temporary change in the bow shock geometry during which similar magnetic and plasma phenomena occur in the upstream region that are observed for the global foreshock during nominal solar wind conditions (see e.g., Kajdič et al., 2017).

To examine further whether the structures constituted transient foreshocks, we study the occurrence of ultra-low-frequency (ULF) fluctuations and ion distributions within the structures. ULF fluctuations from 1 mHz to 1 Hz are regularly observed in the Earth's ion foreshock (e.g., Burgess, 1997; Eastwood, Balogh, et al., 2005; Hobara et al., 2007; Wilson, 2016), and can also be replicated in numerical simulations (e.g., Blanco-Cano et al., 2006; Lin & Wang, 2005; Turc et al., 2018). They are generated through plasma instabilities, such as the left-hand resonant ion beam instability (Gary, 1985), which excites fluctuations around a frequency of 0.1 Hz (a period of 10 s), or the ion-ion beam right-hand instability (Gary, 1991) responsible for generating 30 s fluctuations. These plasma instabilities are triggered by the interactions between backstreaming ions and the incoming solar wind (e.g., Eastwood et al., 2003; Eastwood, Lucek, et al., 2005; Wilson, 2016).

The 30 s ULF fluctuations have been extensively examined (e.g., Greenstadt et al., 1968; Hsieh & Shue, 2013; Palmroth et al., 2015; Turc et al., 2018), their wave periods actually ranging from 10 to ∼55 s depending on the solar wind conditions (Eastwood, Balogh, et al., 2005). Initially transverse fluctuations may develop a significant compressive component (Blanco-Cano et al., 2006; Kajdič et al., 2017; Kis et al., 2004; Omidi et al., 2009; Rojas-Castillo et al., 2013). Moreover, ULF fluctuations in the Earth's ion foreshock often coincide with intermediate, gyrating or gyrophase-bunched ion distributions (Eastwood, Balogh, et al., 2005; Fuselier, 1995; Paschmann et al., 1979). Gyrophase bunching implies a distribution with nonzero mean velocity component perpendicular to the field direction (Fuselier, 1995; Mazelle et al., 2003). Recent studies have shown that when the IMF strength is large (as is the case during ICMEs and their sheath regions), the foreshock can exhibit anomalous features, with in particular the coexistence of 30 s waves at different frequencies, which may be due to coincident multiple ion beams (Turc et al., 2018, 2019). Wavelet power spectra can be used to characterize foreshock wave activity.

Figure 7 shows the magnetic field measurements at C3 for structures (1–3) in panels (a–c) and the Morlet wavelet power spectra for parallel ($B_{\parallel}$) and perpendicular ($B_{\perp}$) fluctuations with respect to the mean magnetic field direction within the structures in panels (d–f) and (g–i), respectively. The $B_{\parallel}$ and $B_{\perp}$ components are defined similarly to Moissard et al. (2019), the perpendicular unit vectors defined as $\mathbf{b_{1,\perp}} = (\mathbf{e_j} \times \mathbf{B_0})/|\mathbf{e_j} \times \mathbf{B_0}|$ and $\mathbf{b_{2,\perp}} = \left(\mathbf{B_0} \times (\mathbf{e_j} \times \mathbf{B_0})\right) / \left(|\mathbf{B_0} \times \mathbf{e_j} \times \mathbf{B_0}|\right)$ where $\mathbf{e_j}$ is chosen from the GSE unit vectors so that the quantity $\|\mathbf{e_j} \times \mathbf{B_0}\|$ is maximized, $\mathbf{B_0}$ being the background magnetic field. The vertical axis indicates the fluctuation period in seconds. In addition, reduced two-dimensional velocity distribution functions (VDF) in the plasma rest frame in the ($V_{\parallel}$, $V_{\perp}$) plane for the structures are shown in Figure 8. The distribution functions are integrated over the second perpendicular direction, with the arrows indicating the bulk direction of the magnetic field and plasma velocity during the structures.

Substantially enhanced power in both parallel and perpendicular fluctuations with periods from 10 to 55 s was found within structures (1) and (2) relative to the surrounding field (Figures 7d–7e and 7g–7h). High power also appeared at shorter periods. For structure (3), the same applies for perpendicular fluctuations (Figure 7i), whereas compressive fluctuation power, while considerable, was not distinguishable from the surroundings (Figure 7f). Higher power at shorter periods is in agreement with previous ULF wave observations: Their frequency is roughly proportional to |B| (Hoppe & Russell, 1982; Turc et al., 2019), which is relatively large for the compressed plasma of ICME sheaths. In addition, Figure 8, where the core plasma is indicated by the large values of the phase space density at the proximity of the centers of the plots, reveals that the two-dimensional VDFs span an extensive region of phase space. The VDFs in particular occupy the bottom-left quadrants implying gyrophase-bunched distributions. The distributions in Figure 8 resemble the disrupted cap distributions seen in numerical simulations where ULF waves are present, which result from backstreaming ions interacting with ULF waves (Kempf et al., 2015).

The C3 observations within the structures do not unambiguously exhibit all standard signatures of a foreshock, such as |B|, V, and n having smaller values in the foreshock than in the upstream solar wind (see e.g., Kajdič et al., 2017). Relative to the surroundings, proton density went up in structure (1) and down in (2), plasma speed decreased in both structure (1) and (2), while density and speed did not change in structure (3) (not shown). The magnetic field magnitude was also higher than their surroundings within all structures. However, an antisunward convected solar wind region, which is bounded by rotational discontinuities in the IMF that temporarily change a portion of the bow shock geometry to quasi-parallel and hosts ULF fluctuations and suprathermal ions, causes so-called traveling foreshock (Kajdič et al., 2017). There were indeed significant changes in field direction at the structure boundaries, with the bow shock becoming quasi-parallel. In addition, the structures occurred in conjunction with notable fluxes of sunward traveling (backstreaming) ions, enhanced power in fluctuations in the

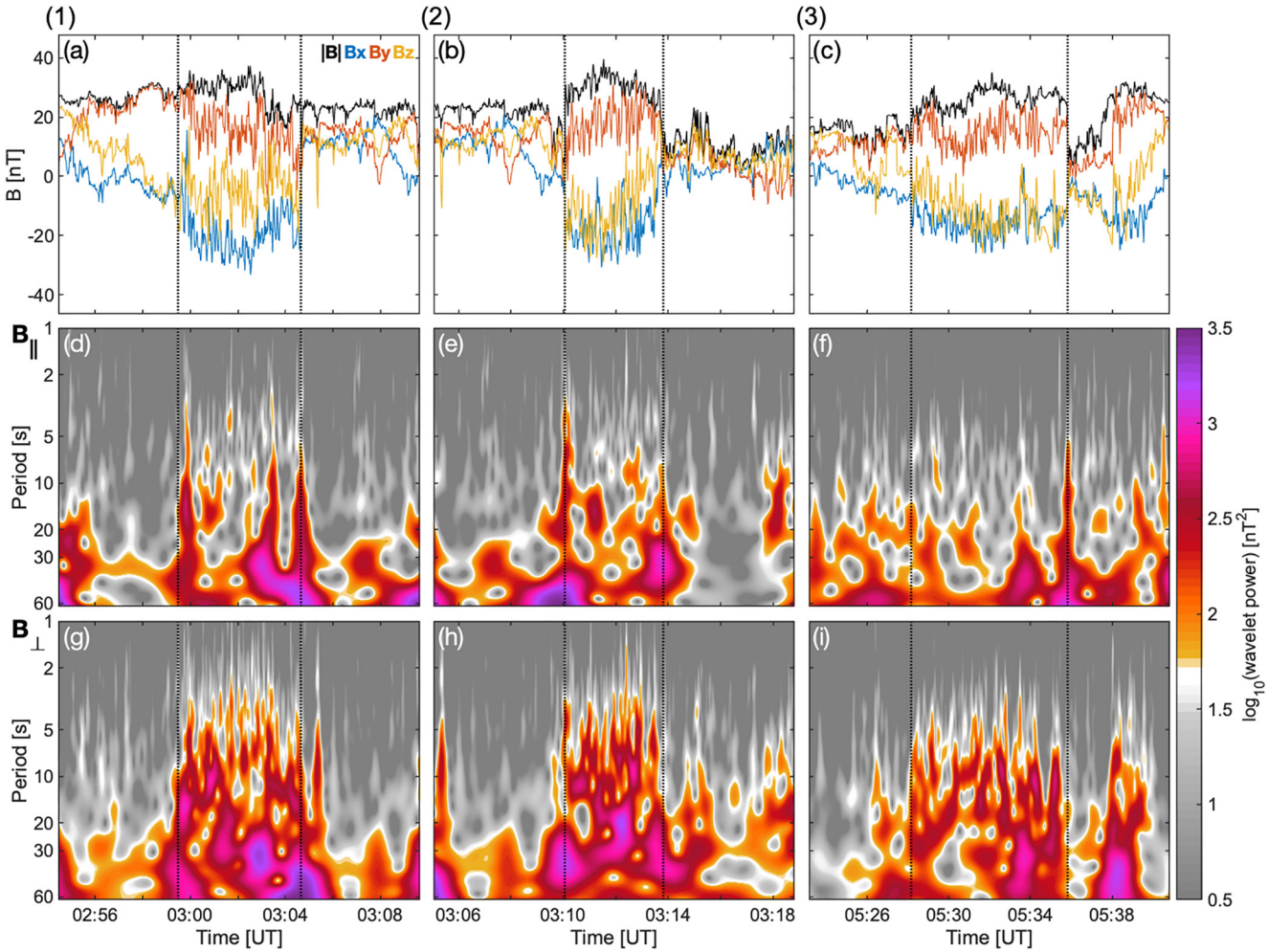

Figure 7. (a–c) C3 magnetic field measurements of structures (1–3), the structure boundaries given by black dotted vertical lines. (d–f) Wavelet power spectrum of magnetic field fluctuations parallel ($B_{\parallel}$) and (g–i) perpendicular ($B_{\perp}$) to the mean field direction within the structures, for the time periods shown in panels (a–c). The power of $B_{\perp}$ is the mean power of the two perpendicular components.

10–55 s period range, and complicated VDFs manifesting gyrating beams. Thus, we conclude that these structures caused traveling foreshocks, during which a transient foreshock occurs upstream of the Earth's bow shock due to a temporary change in the IMF direction. Due to the close separation of the four Cluster spacecraft, we cannot compute the spatial scale of these traveling foreshocks and how local they were (Pfau-Kempf et al., 2016) nor confirm the observation by Kajdič et al. (2017) that the temporal sequence of entry and exit of a traveling foreshock is similar in multiple spacecraft.

To extend the analysis of Section 3 about the transmission of different fluctuations, the wavelet power in the upstream at C3 shown in Figure 7 is compared to the power in the downstream at shown in Figure 9. Compressive and perpendicular fluctuations in Figures 9d–9f and in Figures 9g–9i, respectively, are computed with respect to the mean field direction within the structures in the upstream. Structures (1) and (3) are discernible in Figures 9d and 9g and in Figures 9f and 9i, respectively, which show a significant power within the presumable correspondents of the structures at GT (Figures 9a and 9c). Structure (2) on the other hand is not as distinguishable from the surrounding field in Figures 9b and 9e. However, for all structures (1–3), a large power observed for longer fluctuation periods at C3 in Figure 7 occurred also in the downstream, and in general, the power increased from C3 to GT. The wavelet power was also enhanced for shorter fluctuation periods in the downstream.

For completeness, we plot the wavelet power spectra for the entire ICME sheath passage on 15 May 2005 (Figure 10), which shows the wavelet power of magnetic field magnitude and out-of-ecliptic component for all

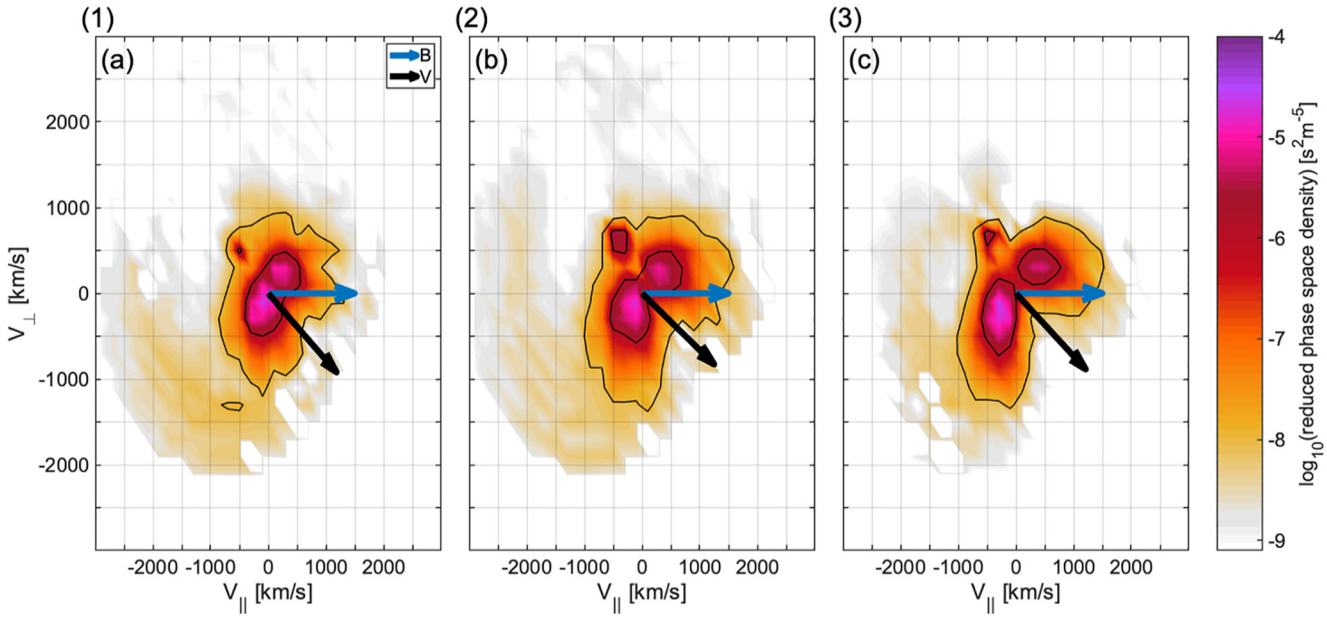

Figure 8. (a–c) Reduced ion velocity distribution functions observed during structures (1–3). The distributions are integrated over the second perpendicular velocity direction and color-coded according to the phase space density. Contours show $\log_{10}$ values of −8 and −6. The horizontal and vertical axes are parallel and perpendicular to the magnetic field direction, which is shown by the blue arrows. The bulk plasma velocity is shown by the black arrow.

spacecraft used in this study. The black dashed (dotted) vertical lines delineate the sheath (structure) boundaries and the black solid curves show the proton cyclotron frequency. The power of |B| and B_z both increased from the upstream to the downstream across a wide range of periods through the entire ICME sheath interval. The structures are discernible in the C3 and GT B_z spectra. Similar observations are made for the B_x and B_y components as for B_z (not shown). It is notable that the highest power of B_z is observed just behind the preceding shock and just in front of the ICME leading edge, consistent with the statistical study by Kilpua et al. (2013). These parts of the sheath are key regions for substorms and geoefficiency (Kalliokoski et al., 2020; Kilpua et al., 2019). This high power of B_z was also detected by ACE and Wind further upstream at L1.

5. Discussion

In this study, we have examined the transmission of structures in an ICME sheath to the Earth's magnetosheath. We focused on the ICME sheath interacting with the magnetosphere on 15 May 2005, that of the driving ejecta having been previously studied by Turc et al. (2014). We paid particular attention to three intervals in the ICME sheath that transmitted from the immediate upstream of the bow shock to the downstream during the ICME sheath passage maintaining their structure. These intervals, labeled structures (1–3), caused traveling foreshocks and were the focus of this study. The structures contained highly southward field component in the upstream region that was amplified significantly in the downstream propagation, increasing their geoeffectiveness. Large amplitude magnetic field fluctuations were present in the structures in both upstream and downstream. Wavelet power in the ULF band and the occurrence of backstreaming ions were examined at the times coinciding with the traveling foreshock structures, and showed intensification especially at higher frequencies as they traveled downstream.

The correlation analysis constructed in this study was in agreement with visual investigation of the spacecraft data, and the identification of the structures in the immediate upstream and downstream was unambiguous. Further in the upstream, in the proximity of L1, the identification of structures (1) and (2) became ambiguous, the ambiguity diminishing at ACE in an additional analysis thus being larger at Wind, which was further away from the Sun-Earth line. On the other hand, a solid identification of structure (3) was made also at L1. Although a large-scale, relatively coherent background magnetic field is embedded in ICME sheaths at 1 AU, they also host local and spatially limited magnetic fluctuations (Ala-Lahti et al., 2020). Our findings are in agreement with this conclusion, especially if structures (1) and (2) were local but steady, long-lived structures already present further

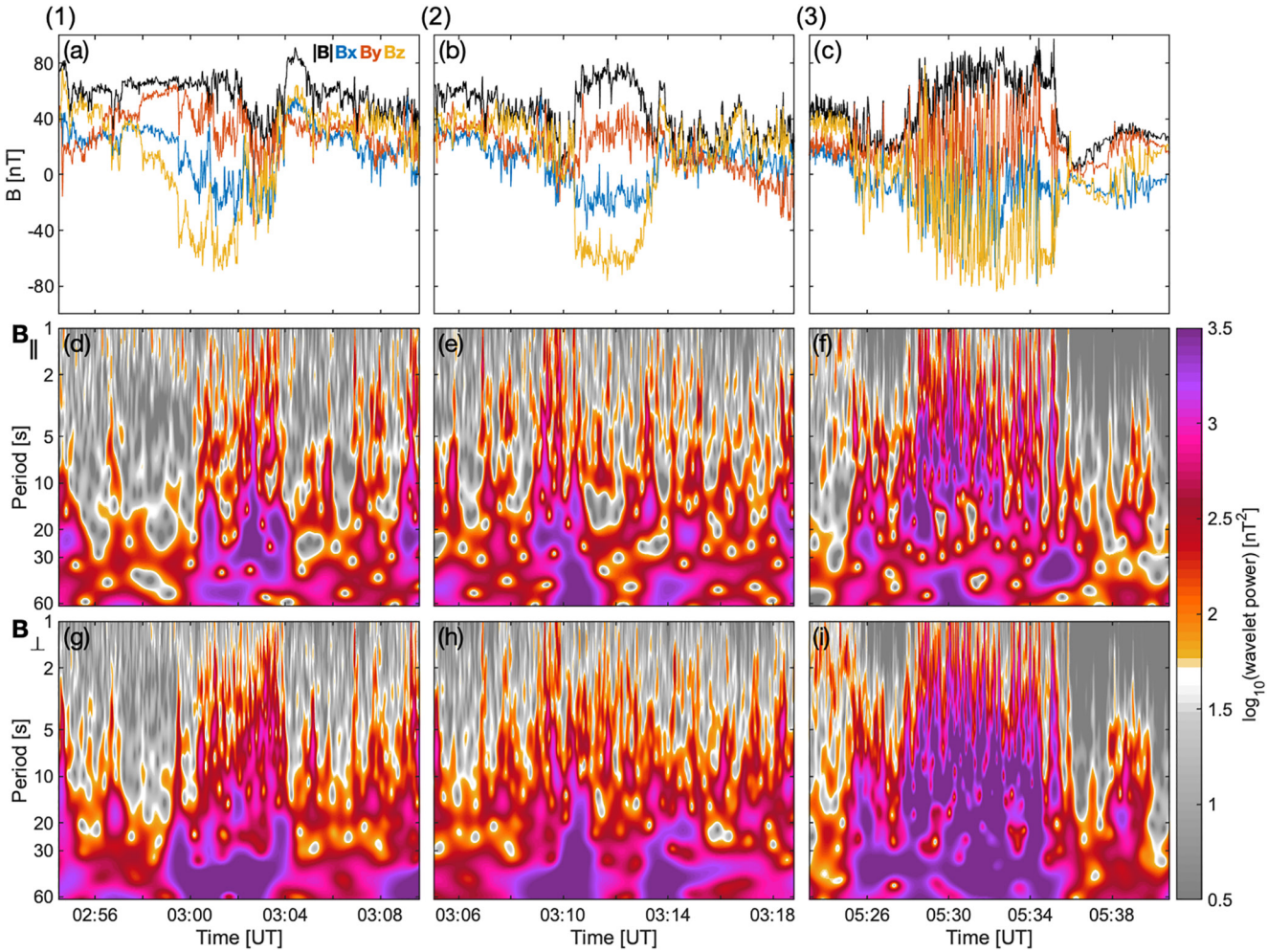

Figure 9. (a–c) Geotail (GT) magnetic field measurements of structures (1–3). (d–f) Wavelet power spectrum of magnetic field fluctuations parallel ($B_{\parallel}$) and (g–i) perpendicular ($B_{\perp}$) to the mean field direction within the structures at C3, for the time periods shown in Figures 7a–7c. The power of $B_{\perp}$ is the mean power of the two perpendicular components.

upstream. Consequently, the chosen solar wind monitor is important when studying the interaction of an ICME sheath with the Earth's magnetosheath. An alternative is that the magnetic field fluctuation properties of ICME sheaths can change relatively quickly with time (i.e., during the propagation time between the spacecraft), even in a manner that is expected to have implications for their space weather response.

Moreover, although our analysis implies that the structures were limited in the longitudinal direction, their extent might have been comparable to the width of the Earth's magnetosheath in the GSE y and z directions. This is consistent with the identification of the structures at ACE data but not at Wind. In such a case, the bow shock angle would differ from the one given in Figure 6 depending on the position in the upstream. Thus, the transmission of the structures into the Earth's magnetosheath might vary along the bow shock due to varying shock configuration and dynamics, which could result in an even more localized occurrence of the structures in the downstream. Our analysis indeed demonstrated that the bow shock angle can experience abrupt changes and quickly adjust to the upstream magnetic field. We showed here that the reaction of the magnetosheath to the upstream field changes is almost immediate. During structures (1–3), the bow shock was in addition quasi-parallel and the structures constituted traveling foreshocks. Although some upstream magnetic fields correlated with the observations in the downstream when the bow shock was quasi-perpendicular, the studied ICME sheath passage had considerable intervals, such as at ~04:30–05:00, when no significant correlations were observed between upstream and downstream measurements.

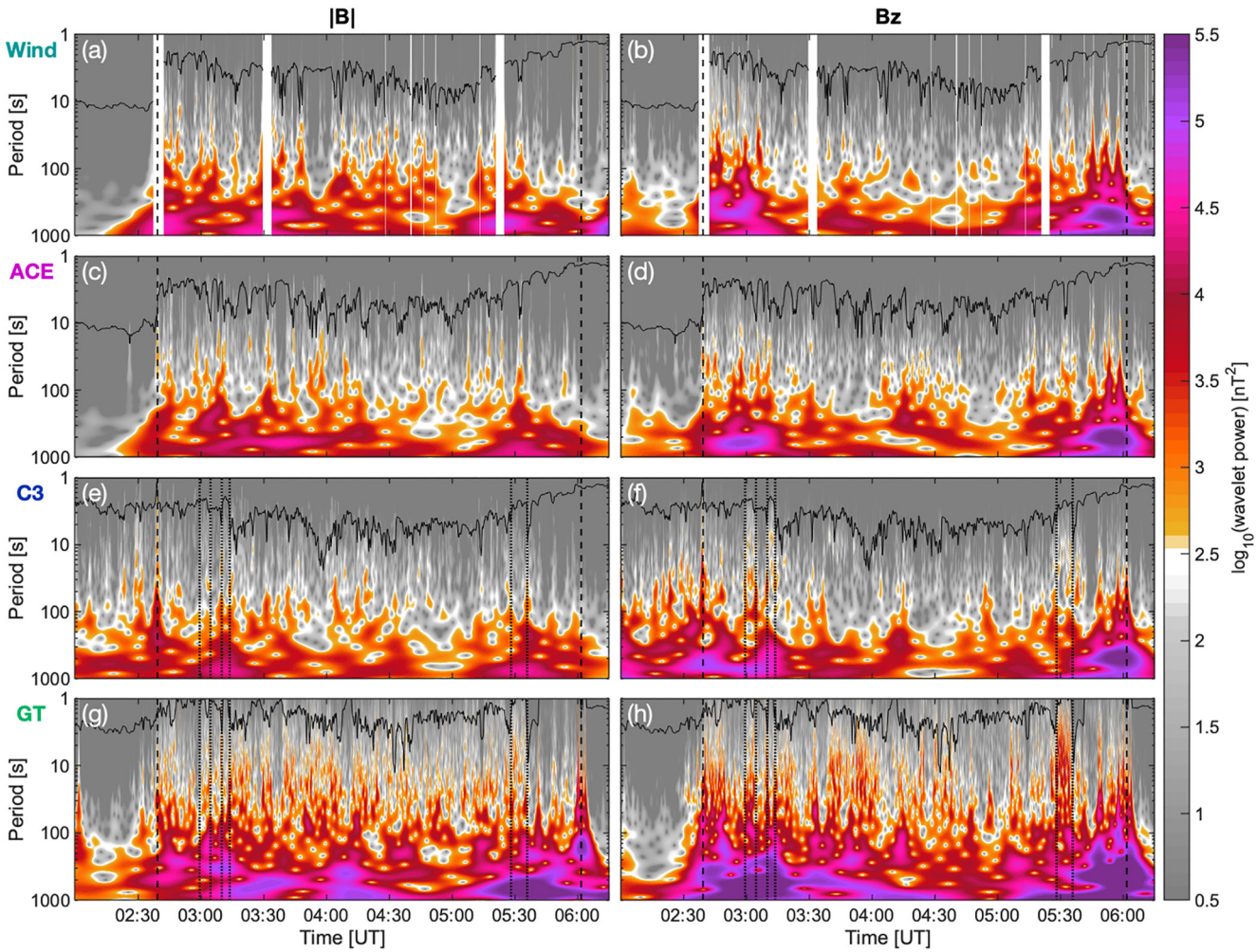

Figure 10. (a–h) Wavelet power spectrum of the magnetic field magnitude and Geocentric Solar Ecliptic (GSE) z component (B_z) during the interplanetary coronal mass ejection (ICME) sheath passage at all spacecraft. The structure boundaries at C3 are marked by the black dotted vertical lines in panels (e–f) and extend to panels (g–h). The black dashed vertical lines give the ICME sheath boundaries. The solid black curves show the ion cyclotron period.

As a consequence of the varying shock dynamics, space weather effects in the inner magnetosphere may be very complicated during an ICME sheath passage. This applies especially for interactions between the magnetopause and southward fields embedded in an ICME sheath, such as structures (1–3) investigated in this study. Magnetic structures in an ICME sheath can indeed excite localized wave generation in the inner magnetosphere (Blum et al., 2021). The above scenario can occur for steady, long-living magnetic structures and for magnetic structures/fluctuations generated while an ICME sheath propagates from L1 to the bow shock.

We found that the probability of the upstream magnetic fields surviving the transmission to the Earth's magnetosheath during the ICME sheath passage was dependent on the frequency of the magnetic fluctuations. Our analysis showed that surviving the transmission became more probable when fluctuations had frequencies below ~0.01 Hz. This is in agreement with previous research (Rakhmanova et al., 2015). We note, however, that waves at higher frequencies are thought to transmit across the bow shock (e.g., Clausen et al., 2009; Takahashi et al., 2021) and more observations are needed for further conclusions.

The traveling foreshocks included fluctuations with periods in the ULF range. These waves were possibly generated by the backstreaming ions in the traveling foreshocks. The lower levels of magnetic fluctuations further in the upstream at L1 is in agreement with this conclusion (assuming the occurrence of the structures already at L1).

The transmission of the ULF fluctuations was not extensively investigated in this study. However, an enhanced wavelet power was observed within structures (1–3) at ULF wave periods in the upstream and downstream, with

a larger power in the downstream that also extended to shorter fluctuation periods. Foreshock ULF waves are considered to be a significant source of magnetospheric fluctuations (Takahashi et al., 1984), which may reach the inner magnetosphere (Francia et al., 2012; Russell et al., 1983; Villante et al., 2011). From this perspective, the magnetic field configurations embedded in ICME sheath fields that form traveling foreshocks and excite the generation of ULF waves result in a complex interplay between an ICME sheath and the Earth's magnetosheath: All fluctuations transmitted from the upstream to the magnetosheath during an ICME sheath passage are not necessarily fluctuations that originated from the solar wind. Instead, an ICME sheath passage may result in bow shock dynamics that generate foreshock ULF waves, which are then transmitted into the magnetosheath. Together with preexisting ICME sheath fluctuations, the generated ULF waves may constitute foreshock turbulence, which can lead to magnetopause reconnection (Chen et al., 2021), thus compounding the space weather impact of the ICME sheath.

The complex interplay together with spacecraft locations may actually explain the low correlation at higher frequencies in Figure 5. As discussed above, longitudinally (and latitudinally) extended structures that are observed in the upstream, such as structures (1–3), modify the shock configuration. Because of this and of the shock curvature, their interaction with the shock, and a possible foreshock, will vary with space and time. In addition, fluctuations within them may evolve due to the dynamics of the ICME sheath itself, or that of the traveling foreshock, before the structures enter the downstream. For example, ULF fluctuations excited within a structure entering the magnetosheath flank have more time to develop a compressive component than if the structure crossed the bow shock closer to the Sun-Earth line. ULF waves within a lasting foreshock region can further deepen, forming shocklets and short-large-amplitude magnetic structures (e.g., Kajdič et al., 2017, and references therein). Foreshock waves have also a shorter longitudinal extent when present inside a driver, which has higher |B| than more typical solar wind (Archer et al., 2005; Turc et al., 2018, 2019). Consequently, fluctuations at higher frequencies can differ substantially from each other between the upstream observation location and their bow shock crossing location that precedes their subsequent downstream observation location, whereas extended larger-scale structures may be preserved from the upstream to the downstream being observed by spacecraft that are not radially aligned. This scenario is applicable for the entire ICME sheath passage, during which the spacecraft separation in the GSE yz-plane between C3 and GT varied between 6.5 and 7.5 R_E. In addition, the magnetosheath dynamics during the ICME sheath passage could have modified fluctuations properties at higher frequencies during the traveling time from C3 to GT, which had a spacecraft separation in the GSE x-direction between 1.0 and 4.6 R_E during the event.

Finally, structures (1–2) might have originated from magnetic field fluctuations pre-existing in the solar wind that were swept by the ICME sheath (see e.g., Tsurutani et al., 1988). Such pre-existing fluctuations experience shock compression twice: First when entering the ICME sheath and second when the ICME sheath transmits to the Earth's magnetosheath. Alternatively, the structures could have been generated by the in situ dynamics of the turbulent plasma downstream of an interplanetary shock. The downstream turbulence is dependent on conditions in the preceding solar wind (see e.g., Pitňa et al., 2016, 2021; Zank et al., 2021). These scenarios also emphasize the importance of understanding the dynamics of the solar wind. Successive observations of the same ICME sheath by multiple spacecraft with relatively small separations would improve our understanding of these origins. Solar Orbiter and Parker Solar Probe will provide opportunities to investigate if these structures are present closer to the Sun.

Structure (3) and the coinciding large-scale field variations at the back of the ICME sheath observed by all spacecraft could have emanated from field line draping around the driving ejecta (e.g., Gosling & McComas, 1987; McComas et al., 1989; Tsurutani et al., 1988). As discussed by Jones et al. (2002), the orientations of the constituent magnetic fields accreting at the back of the ICME sheath should remain tangential to the local leading surface of the driving ejecta. This accretion can form periods of organized layers of magnetic fields known as planar magnetic structures (Nakagawa et al., 1989). The occurrence of planar magnetic structures in the ICME sheath observed at 1 AU on 15 May 2005 was investigated by Palmerio et al. (2016), and interestingly, the authors reported a planar magnetic structure only in the mid-sheath. We note that the identification was performed with Wind data, which had a significant data gap during structure (3), and that deviations from the general field line draping pattern can occur (Kaymaz & Siscoe, 2006). Large-scale field variations at the back of the ICME sheath can also result from the erosion of the ICME ejecta (Dasso et al., 2006; Lavraud et al., 2014; Manchester et al., 2014; Ruffenach et al., 2012).

ICME sheaths and their interplay with the Earth's magnetosphere constitute an intriguing coupled system. We highlight, together with the work by Ala-Lahti et al. (2020) and by Blum et al. (2021), the importance that the fine structure of sheath fields have in this interplay. Predicting ICME sheath structures and properties that are relevant for space weather and geoefficiency can be particularly challenging due to the complex dynamics of ICME sheaths, which can vary with propagation from the Sun. The magnetic fine structure observed at L1 might not always match reality at the Earth due to the spacecraft location or due to the evolution of the fluctuations. This is important for space weather predictions that are dependent on observations at L1.

Data Availability Statement

ACE and Wind data used in this study are available at the NASA Goddard Space Flight Center Coordinated Data Analysis Web (CDAWeb, http://cdaweb.gsfc.nasa.gov/). The investigated magnetic field (plasma) data were measured by the ACE and Wind Magnetic Fields Investigation (ACE Solar Wind Electron Proton Alpha Monitor and Wind Solar Wind Experiment) instruments. The ACE and Wind data sources and their documentation are given by California Institute of Technology (http://www.srl.caltech.edu/ACE/) and NASA (https://wind.nasa.gov/data.php). Cluster data analyzed in this study were obtained from the Cluster Science Archive (https://csa.esac.esa.int/csa-web/). Magnetic field (plasma) data from the Cluster Fluxgate Magnetometer (Ion Spectrometry) instrument were investigated. The Cluster data sources and their documentation are given by ESA (https://www.cosmos.esa.int/web/csa/). Geotail data analyzed in this study were obtained from Data ARchives and Transmission System (DARTS), provided by Center for Science-satellite Operation and Data Archive (C-SODA) at ISAS/JAXA (https://darts.isas.jaxa.jp/stp/geotail/data). Magnetic field (plasma) data from the Geotail Magnetic Field Experiment (Low Energy Particle Experiment) instruments were investigated. The Geotail data sources and their documentation are given by DARTS (https://darts.isas.jaxa.jp/stp/geotail/).

Acknowledgments
The authors thank the sources for providing data. M. Ala-Lahti, E. Kilpua, S. W. Good, and L. Turc acknowledge The Finnish Centre of Excellence in Research of Sustainable Space, funded through the Academy of Finland Grant 312390. M. Ala-Lahti, E. Kilpua, and S. W. Good also acknowledge Academy of Finland Project 310445 (SMASH). This project has received funding from the European Research Council (ERC) under the European Union's Horizon 2020 research and innovation program (grant agreement 724391, SolMAG). A. P. Dimmock received financial support from the Swedish National Space Agency (grant 2020-00111). The work by T. I. Pulkkinen is supported by Academy of Finland grant 310444 and NSF grant 2033563. E. Yordanova research was funded by the Swedish Civil Contingencies Agency (grant 2016-2021) and SNSA (grant 86/20). The work of L. Turc is supported by the Academy of Finland (grant number 322544) and the University of Helsinki (3-year research grant 2020-2022). The authors also wish to thank the two anonymous reviewers, whose constructive comments have lead to a much improved manuscript.

References

Ala-Lahti, M., Ruohotie, J., Good, S., Kilpua, E. K. J., & Lugaz, N. (2020). Spatial coherence of interplanetary coronal mass ejection sheaths at 1 AU. *Journal of Geophysical Research: Space Physics*, *125*(9), e28002. https://doi.org/10.1029/2020JA028002

Alexander, R. A. (1990). A note on averaging correlations. *Bulletin of the Psychonomic Society*, *28*(4), 335–336. https://doi.org/10.3758/BF03334037

Archer, M., Horbury, T. S., Lucek, E. A., Mazelle, C., Balogh, A., & Dandouras, I. (2005). Size and shape of ULF waves in the terrestrial foreshock. *Journal of Geophysical Research: Space Physics*, *110*(A5), A05208. https://doi.org/10.1029/2004JA010791

Balogh, A., Dunlop, M. W., Cowley, S. W. H., Southwood, D. J., Thomlinson, J. G., Glassmeier, K. H., et al. (1997). The cluster magnetic field investigation. *Space Science Reviews*, *79*, 65–91. https://doi.org/10.1023/a:1004970907748

Bisi, M. M., Breen, A. R., Jackson, B. V., Fallows, R. A., Walsh, A. P., Mikić, Z., et al. (2010). From the Sun to the Earth: The 13 May 2005 coronal mass ejection. *Solar Physics*, *265*(1–2), 49–127. https://doi.org/10.1007/s11207-010-9602-8

Blanco-Cano, X., Kajdič, P., Aguilar-Rodríguez, E., Russell, C. T., Jian, L. K., & Luhmann, J. G. (2016). Interplanetary shocks and foreshocks observed by STEREO during 2007-2010. *Journal of Geophysical Research: Space Physics*, *121*(2), 992–1008. https://doi.org/10.1002/2015JA021645

Blanco-Cano, X., Omidi, N., & Russell, C. T. (2006). Macrostructure of collisionless bow shocks: 2. ULF waves in the foreshock and magnetosheath. *Journal of Geophysical Research*, *111*(A10), A10205. https://doi.org/10.1029/2005JA011421

Blum, L. W., Koval, A., Richardson, I. G., Wilson, L. B., Malaspina, D., Greeley, A., & Jaynes, A. N. (2021). Prompt response of the dayside magnetosphere to discrete structures within the sheath region of a coronal mass ejection. *Geophysical Research Letters*, *48*(11), e92700. https://doi.org/10.1029/2021GL092700

Boudouridis, A., Zesta, E., Lyons, L. R., Anderson, P. C., & Lummerzheim, D. (2005). Enhanced solar wind geoeffectiveness after a sudden increase in dynamic pressure during southward IMF orientation. *Journal of Geophysical Research: Space Physics*, *110*(A5), A05214. https://doi.org/10.1029/2004JA010704

Burgess, D. (1997). What do we really know about upstream waves? *Advances in Space Research*, *20*(4–5), 673–682. https://doi.org/10.1016/S0273-1177(97)00455-9

Burton, R. K., McPherron, R. L., & Russell, C. T. (1975). An empirical relationship between interplanetary conditions and Dst. *Journal of Geophysical Research*, *80*(31), 4204. https://doi.org/10.1029/JA080i031p04204

Chen, L.-J., Ng, J., Omelchenko, Y., & Wang, S. (2021). Magnetopause Reconnection and Indents Induced by Foreshock Turbulence. *Geophysical Research Letters*, *48*(11), e93029. https://doi.org/10.1029/2021GL093029

Clausen, L. B. N., Yeoman, T. K., Fear, R. C., Behlke, R., Lucek, E. A., & Engebretson, M. J. (2009). First simultaneous measurements of waves generated at the bow shock in the solar wind, the magnetosphere and on the ground. *Annales Geophysicae*, *27*(1), 357–371. https://doi.org/10.5194/angeo-27-357-2009

Crooker, N. U. (2000). Solar and heliospheric geoeffective disturbances. *Journal of Atmospheric and Solar-Terrestrial Physics*, *62*(12), 1071–1085. https://doi.org/10.1016/S1364-6826(00)00098-5

Dasso, S., Mandrini, C. H., Démoulin, P., & Luoni, M. L. (2006). A new model-independent method to compute magnetic helicity in magnetic clouds. *Astronomy and Astrophysics*, *455*(1), 349–359. https://doi.org/10.1051/0004-6361:20064806

Dasso, S., Mandrini, C. H., Schmieder, B., Cremades, H., Cid, C., Cerrato, Y., et al. (2009). Linking two consecutive nonmerging magnetic clouds with their solar sources. *Journal of Geophysical Research: Space Physics*, *114*(A2), A02109. https://doi.org/10.1029/2008JA013102

Dimmock, A. P., Rosenqvist, L., Hall, J. O., Viljanen, A., Yordanova, E., Honkonen, I., & Sjöberg, E. C. (2019). The GIC and geomagnetic response over Fennoscandia to the 7-8 September 2017 geomagnetic storm. *Space Weather*, *17*(7), 989–1010. https://doi.org/10.1029/2018SW002132

Eastwood, J. P., Balogh, A., Lucek, E. A., Mazelle, C., & Dandouras, I. (2003). On the existence of Alfvén waves in the terrestrial foreshock. *Annales Geophysicae*, *21*(7), 1457–1465. https://doi.org/10.5194/angeo-21-1457-2003

Eastwood, J. P., Balogh, A., Lucek, E. A., Mazelle, C., & Dandouras, I. (2005). Quasi-monochromatic ULF foreshock waves as observed by the four-spacecraft Cluster mission: 1. Statistical properties. *Journal of Geophysical Research*, *110*(A11), A11219. https://doi.org/10.1029/2004JA010617

Eastwood, J. P., Lucek, E. A., Mazelle, C., Meziane, K., Narita, Y., Pickett, J., & Treumann, R. A. (2005). The foreshock. *Space Science Reviews*, *118*(1–4), 41–94. https://doi.org/10.1007/s11214-005-3824-3

Fox, N. J., Velli, M. C., Bale, S. D., Decker, R., Driesman, A., Howard, R. A., et al. (2016). The Solar Probe Plus mission: Humanity's first visit to our star. *Space Science Reviews*, *204*(1–4), 7–48. https://doi.org/10.1007/s11214-015-0211-6

Francia, P., Regi, M., De Lauretis, M., Villante, U., & Pilipenko, V. A. (2012). A case study of upstream wave transmission to the ground at polar and low latitudes. *Journal of Geophysical Research: Space Physics*, *117*(A1), A01210. https://doi.org/10.1029/2011JA016751

Fuselier, S. A. (1995). Ion distributions in the Earth's foreshock upstream from the bow shock. *Advances in Space Research*, *15*(8–9), 43–52. https://doi.org/10.1016/0273-1177(94)00083-D

Gary, S. P. (1985). Electromagnetic ion beam instabilities: Hot beams at interplanetary shocks. *The Astrophysical Journal*, *288*, 342–352. https://doi.org/10.1086/162797

Gary, S. P. (1991). Electromagnetic ion/ion instabilities and their consequences in space plasmas: A review. *Space Science Reviews*, *56*(3–4), 373–415. https://doi.org/10.1007/BF00196632

Gonzalez, W. D., Echer, E., Tsurutani, B. T., Clúa de Gonzalez, A. L., & Dal Lago, A. (2011). Interplanetary origin of intense, superintense and extreme geomagnetic storms. *Space Science Reviews*, *158*(1), 69–89. https://doi.org/10.1007/s11214-010-9715-2

Gonzalez, W. D., Tsurutani, B. T., & Clúa de Gonzalez, A. L. (1999). Interplanetary origin of geomagnetic storms. *Space Science Reviews*, *88*, 529–562. https://doi.org/10.1023/A:1005160129098

Good, S. W., Ala-Lahti, M., Palmerio, E., Kilpua, E. K. J., & Osmane, A. (2020). Radial evolution of magnetic field fluctuations in an interplanetary coronal mass ejection sheath. *The Astrophysical Journal*, *893*(2), 110. https://doi.org/10.3847/1538-4357/ab7fa2

Good, S. W., Forsyth, R. J., Eastwood, J. P., & Möstl, C. (2018). Correlation of ICME magnetic fields at radially aligned spacecraft. *Solar Physics*, *293*(3), 52. https://doi.org/10.1007/s11207-018-1264-y

Good, S. W., Kilpua, E. K. J., LaMoury, A. T., Forsyth, R. J., Eastwood, J. P., & Möstl, C. (2019). Self-similarity of ICME flux ropes: Observations by radially aligned spacecraft in the inner heliosphere. *Journal of Geophysical Research: Space Physics*, *124*(7), 4960–4982. https://doi.org/10.1029/2019JA026475

Gosling, J. T., & McComas, D. J. (1987). Field line draping about fast coronal mass ejecta: A source of strong out-of-the-ecliptic interplanetary magnetic fields. *Geophysical Research Letters*, *14*(4), 355–358. https://doi.org/10.1029/GL014i004p00355

Greenstadt, E. W., Green, I. M., Inouye, G. T., Hundhausen, A. J., Bame, S. J., & Strong, I. B. (1968). Correlated magnetic field and plasma observations of the Earth's bow shock. *Journal of Geophysical Research*, *73*(1), 51. https://doi.org/10.1029/JA073i001p00051

Hietala, H., Kilpua, E. K. J., Turner, D. L., & Angelopoulos, V. (2014). Depleting effects of ICME-driven sheath regions on the outer electron radiation belt. *Geophysical Research Letters*, *41*(7), 2258–2265. https://doi.org/10.1002/2014GL059551

Hobara, Y., Walker, S. N., Balikhin, M., Pokhotelov, O. A., Dunlop, M., Nilsson, H., & RèMe, H. (2007). Characteristics of terrestrial foreshock ULF waves: Cluster observations. *Journal of Geophysical Research: Space Physics*, *112*(A7), A07202. https://doi.org/10.1029/2006JA012142

Hoppe, M. M., & Russell, C. T. (1982). Particle acceleration at planetary bow shock waves. *Nature*, *295*(5844), 41–42. https://doi.org/10.1038/295041a0

Hsieh, W. C., & Shue, J. H. (2013). Dependence of the oblique propagation of ULF foreshock waves on solar wind parameters. *Journal of Geophysical Research: Space Physics*, *118*(7), 4151–4160. https://doi.org/10.1002/jgra.50225

Huttunen, K. E. J., Kilpua, S. P., Pulkkinen, A., Viljanen, A., & Tanskanen, E. (2008). Solar wind drivers of large geomagnetically induced currents during the solar cycle 23. *Space Weather*, *6*(10), S10002. https://doi.org/10.1029/2007SW000374

Huttunen, K. E. J., & Koskinen, H. E. J. (2004). Importance of post-shock streams and sheath region as drivers of intense magnetospheric storms and high-latitude activity. *Annales Geophysicae*, *22*(5), 1729–1738. https://doi.org/10.5194/angeo-22-1729-2004

Huttunen, K. E. J., Koskinen, H. E. J., & Schwenn, R. (2002). Variability of magnetospheric storms driven by different solar wind perturbations. *Journal of Geophysical Research: Space Physics*, *107*(A7), 1121. https://doi.org/10.1029/2001JA900171

Janvier, M., Winslow, R. M., Good, S., Bonhomme, E., Démoulin, P., Dasso, S., & Boakes, P. D. (2019). Generic magnetic field intensity profiles of interplanetary coronal mass ejections at Mercury, Venus, and Earth from superposed epoch analyses. *Journal of Geophysical Research (Space Physics)*, *124*(2), 812–836. https://doi.org/10.1029/2018JA025949

Jones, G. H., Rees, A., Balogh, A., & Forsyth, R. J. (2002). The draping of heliospheric magnetic fields upstream of coronal mass ejecta. *Geophysical Research Letters*, *29*(11), 1520. https://doi.org/10.1029/2001GL014110

Kajdič, P., Blanco-Cano, X., Omidi, N., Rojas-Castillo, D., Sibeck, D. G., & Billingham, L. (2017). Traveling Foreshocks and Transient Foreshock Phenomena. *Journal of Geophysical Research: Space Physics*, *122*(9), 9148–9168. https://doi.org/10.1002/2017JA023901

Kajdič, P., Preisser, L., Blanco-Cano, X., Burgess, D., & Trotta, D. (2019). First observations of irregular surface of interplanetary shocks at ion scales by Cluster. *The Astrophysical Journal Letters*, *874*(2), L13. https://doi.org/10.3847/2041-8213/ab0e84

Kalliokoski, M. M. H., Kilpua, E. K. J., Osmane, A., Turner, D. L., Jaynes, A. N., Turc, L., & Palmroth, M. (2020). Outer radiation belt and inner magnetospheric response to sheath regions of coronal mass ejections: A statistical analysis. *Annales Geophysicae*, *38*(3), 683–701. https://doi.org/10.5194/angeo-38-683-2020

Kaymaz, Z., & Siscoe, G. (2006). Field-line draping around ICMES. *Solar Physics*, *239*(1–2), 437–448. https://doi.org/10.1007/s11207-006-0308-x

Kempf, Y., Pokhotelov, D., Gutynska, O., Wilson III, L. B., Walsh, B. M., von Alfthan, S., et al. (2015). Ion distributions in the Earth's foreshock: Hybrid-Vlasov simulation and THEMIS observations. *Journal of Geophysical Research: Space Physics*, *120*(5), 3684–3701. https://doi.org/10.1002/2014ja020519

Kilpua, E. K. J., Balogh, A., von Steiger, R., & Liu, Y. D. (2017). Geoeffective properties of solar transients and stream interaction regions. *Space Science Reviews*, *212*(3–4), 1271–1314. https://doi.org/10.1007/s11214-017-0411-3

Kilpua, E. K. J., Fontaine, D., Moissard, C., Ala-Lahti, M., Palmerio, E., Yordanova, E., & Turc, L. (2019). Solar wind properties and geospace impact of coronal mass ejection-driven sheath regions: Variation and driver dependence. *Space Weather*, *17*(8), 1257–1280. https://doi.org/10.1029/2019SW002217

Kilpua, E. K. J., Hietala, H., Koskinen, H. E. J., Fontaine, D., & Turc, L. (2013). Magnetic field and dynamic pressure ULF fluctuations in coronal-mass-ejection-driven sheath regions. *Annales Geophysicae*, *31*(9), 1559–1567. https://doi.org/10.5194/angeo-31-1559-2013

Kilpua, E. K. J., Koskinen, H. E. J., & Pulkkinen, T. I. (2017). Coronal mass ejections and their sheath regions in interplanetary space. *Living Reviews in Solar Physics*, *14*(1), 5. https://doi.org/10.1007/s41116-017-0009-6

Kis, A., Scholer, M., Klecker, B., Möbius, E., Lucek, E. A., Rème, H., et al. (2004). Multi-spacecraft observations of diffuse ions upstream of Earth's bow shock. *Geophysical Research Letters*, *31*(20), L20801. https://doi.org/10.1029/2004GL020759

Knipp, D., Kilcommons, L., Hunt, L., Mlynczak, M., Pilipenko, V., Bowman, B., & Drake, K. (2013). Thermospheric damping response to sheath-enhanced geospace storms. *Geophysical Research Letters*, *40*(7), 1263–1267. https://doi.org/10.1002/grl.50197

Kokubun, S., Yamamoto, T., Acuña, M. H., Hayashi, K., Shiokawa, K., & Kawano, H. (1994). The GEOTAIL magnetic field experiment. *Journal of Geomagnetism and Geoelectricity*, *46*(1), 7–21. https://doi.org/10.5636/jgg.46.7

Lavraud, B., Ruffenach, A., Rouillard, A. P., Kajdic, P., Manchester, W. B., & Lugaz, N. (2014). Geo-effectiveness and radial dependence of magnetic cloud erosion by magnetic reconnection. *Journal of Geophysical Research: Space Physics*, *119*(1), 26–35. https://doi.org/10.1002/2013JA019154

Lepping, R. P., Acũna, M. H., Burlaga, L. F., Farrell, W. M., Slavin, J. A., Schatten, K. H., & Worley, E. M. (1995). The wind magnetic field investigation. *Space Science Reviews*, *71*, 207–229. https://doi.org/10.1007/BF00751330

Lin, Y., & Wang, X. Y. (2005). Three-dimensional global hybrid simulation of dayside dynamics associated with the quasi-parallel bow shock. *Journal of Geophysical Research*, *110*(A12), A12216. https://doi.org/10.1029/2005JA011243

Lindsay, G. M., Russell, C. T., & Luhmann, J. G. (1995). Coronal mass ejection and stream interaction region characteristics and their potential geomagnetic effectiveness. *Journal of Geophysical Research: Space Physics*, *100*(A9), 16999–17014. https://doi.org/10.1029/95JA00525

Lugaz, N., Farrugia, C. J., Winslow, R. M., Al-Haddad, N., Galvin, A. B., Nieves-Chinchilla, T., et al. (2018). On the spatial coherence of magnetic ejecta: Measurements of coronal mass ejections by multiple spacecraft longitudinally separated by 0.01 AU. *The Astrophysical Journal Letters*, *864*(1), L7. https://doi.org/10.3847/2041-8213/aad9f4

Lugaz, N., Farrugia, C. J., Winslow, R. M., Al-Haddad, N., Kilpua, E. K. J., & Riley, P. (2016). Factors affecting the geoeffectiveness of shocks and sheaths at 1 AU. *Journal of Geophysical Research: Space Physics*, *121*(1110), 10861–10879. https://doi.org/10.1002/2016JA023100

Lugaz, N., Winslow, R. M., & Farrugia, C. J. (2020). Evolution of a long-duration coronal mass ejection and its sheath region between Mercury and Earth on 9-14 July 2013. *Journal of Geophysical Research: Space Physics*, *125*(1), e27213. https://doi.org/10.1029/2019JA027213

Luhmann, J. G., Gopalswamy, N., Jian, L. K., & Lugaz, N. (2020). ICME evolution in the inner heliosphere. *Solar Physics*, *295*(4), 61. https://doi.org/10.1007/s11207-020-01624-0

Manchester, W. B., Kilpua, E. K. J., Liu, Y. D., Lugaz, N., Riley, P., Török, T., & Vršnak, B. (2017). The physical processes of CME/ICME evolution. *Space Science Reviews*, *212*(3–4), 1159–1219. https://doi.org/10.1007/s11214-017-0394-0

Manchester, W. B., Kozyra, J. U., Lepri, S. T., & Lavraud, B. (2014). Simulation of magnetic cloud erosion during propagation. *Journal of Geophysical Research: Space Physics*, *119*(7), 5449–5464. https://doi.org/10.1002/2014JA019882

Mazelle, C., Meziane, K., Le Quéau, D., Wilber, M., Eastwood, J. P., Rème, H., et al. (2003). Production of gyrating ions from nonlinear wave-particle interaction upstream from the Earth's bow shock: A case study from Cluster-CIS. *Planetary and Space Science*, *51*(12), 785–795. https://doi.org/10.1016/j.pss.2003.05.002

McComas, D. J., Bame, S. J., Barker, P., Feldman, W. C., Phillips, J. L., Riley, P., & Griffee, J. W. (1998). Solar wind electron proton alpha monitor (SWEPAM) for the Advanced Composition Explorer. *Space Science Reviews*, *86*, 563–612. https://doi.org/10.1023/A:1005040232597

McComas, D. J., Gosling, J. T., Bame, S. J., Smith, E. J., & Cane, H. V. (1989). A test of magnetic field draping induced B_z perturbations ahead of fast coronal mass ejecta. *Journal of Geophysical Research: Space Physics*, *94*(A2), 1465–1471. https://doi.org/10.1029/JA094iA02p01465

Meng, X., Tsurutani, B. T., & Mannucci, A. J. (2019). The solar and interplanetary causes of superstorms (minimum Dst ≤ -250 nT) during the space age. *Journal of Geophysical Research: Space Physics*, *124*(6), 3926–3948. https://doi.org/10.1029/2018JA026425

Merka, J., Szabo, A., Slavin, J. A., & Peredo, M. (2005). Three-dimensional position and shape of the bow shock and their variation with upstream Mach numbers and interplanetary magnetic field orientation. *Journal of Geophysical Research: Space Physics*, *110*(A4), A04202. https://doi.org/10.1029/2004JA010944

Moissard, C., Fontaine, D., & Savoini, P. (2019). A study of fluctuations in magnetic cloud-driven sheaths. *Journal of Geophysical Research: Space Physics*, *124*(11), 8208–8226. https://doi.org/10.1029/2019JA026952

Mukai, T., Machida, S., Saito, Y., Hirahara, M., Terasawa, T., Kaya, N., & Nishida, A. (1994). The low energy particle (LEP) experiment onboard the GEOTAIL satellite. *Journal of Geomagnetism and Geoelectricity*, *46*(8), 669–692. https://doi.org/10.5636/jgg.46.669

Müller, D., Marsden, R. G., St. Cyr, O. C., Gilbert, H. R., & The Solar Orbiter Team. (2013). Solar Orbiter: Exploring the sun-heliosphere connection. *Solar Physics*, *285*(1–2), 25–70. https://doi.org/10.1007/s11207-012-0085-7

Nakagawa, T., Nishida, A., & Saito, T. (1989). Planar magnetic structures in the solar wind. *Journal of Geophysical Research: Space Physics*, *94*(A9), 11761–11775. https://doi.org/10.1029/JA094iA09p11761

Nykyri, K., Bengtson, M., Angelopoulos, V., Nishimura, Y., & Wing, S. (2019). Can enhanced flux loading by high-speed jets lead to a substorm? Multipoint detection of the christmas day substorm onset at 08:17 UT, 2015. *Journal of Geophysical Research: Space Physics*, *124*(6), 4314–4340. https://doi.org/10.1029/2018JA026357

Ogilvie, K. W., Chornay, D. J., Fritzenreiter, R. J., Hunsaker, F., Keller, J., Lobell, J., & Gergin, E. (1995). SWE, a comprehensive plasma instrument for the wind spacecraft. *Space Science Reviews*, *71*, 55–77. https://doi.org/10.1007/BF00751326

Oliveira, D. M., & Samsonov, A. A. (2018). Geoeffectiveness of interplanetary shocks controlled by impact angles: A review. *Advances in Space Research*, *61*(1), 1–44. https://doi.org/10.1016/j.asr.2017.10.006

Olkin, I., & Pratt, J. W. (1958). Unbiased estimation of certain correlation coefficients. *The Annals of Mathematical Statistics*, *29*(1), 201–211. https://doi.org/10.1214/aoms/1177706717

Omidi, N., Sibeck, D. G., & Blanco-Cano, X. (2009). Foreshock compressional boundary. *Journal of Geophysical Research: Space Physics*, *114*(A8), A08205. https://doi.org/10.1029/2008JA013950

Palmerio, E., Kilpua, E. K. J., & Savani, N. P. (2016). Planar magnetic structures in coronal mass ejection-driven sheath regions. *Annales Geophysicae*, *34*(2), 313–322. https://doi.org/10.5194/angeo-34-313-2016

Palmroth, M., Archer, M., Vainio, R., Hietala, H., Pfau-Kempf, Y., Hoilijoki, S., et al. (2015). ULF foreshock under radial IMF: THEMIS observations and global kinetic simulation Vlasiator results compared. *Journal of Geophysical Research: Space Physics*, *120*(10), 8782–8798. https://doi.org/10.1002/2015JA021526

Paschmann, G., & Daly, P. W. (1998). Analysis methods for multi-spacecraft data. *ISSI scientific reports series SR-001, ESA/ISSI, vol. 1, ISBN 1608-280X, 1998*.

Paschmann, G., Sckopke, N., Bame, S. J., Asbridge, J. R., Gosling, J. T., Russell, C. T., & Greenstadt, E. W. (1979). Association of low-frequency waves with suprathermal ions in the upstream solar wind. *Geophysical Research Letters*, *6*(3), 209–212. https://doi.org/10.1029/GL006i003p00209

Pfau-Kempf, Y., Hietala, H., Milan, S. E., Juusola, L., Hoilijoki, S., Ganse, U., & Palmroth, M. (2016). Evidence for transient, local ion foreshocks caused by dayside magnetopause reconnection. *Annales Geophysicae*, *34*(11), 943–959. https://doi.org/10.5194/angeo-34-943-2016

Pitňa, A., Šafránková, J., Němeček, Z., Ďurovcová, T., & Kis, A. (2021). Turbulence upstream and downstream of interplanetary shocks. *Frontiers in Physics*, *8*, 654. https://doi.org/10.3389/fphy.2020.626768

Pitňa, A., Šafránková, J., Němeček, Z., Goncharov, O., Němec, F., Přech, L., & Zastenker, G. N. (2016). Density fluctuations upstream and downstream of interplanetary shocks. *The Astrophysical Journal*, *819*(1), 41. https://doi.org/10.3847/0004-637X/819/1/41

Pulkkinen, T. I., Partamies, N., Huttunen, K. E. J., Reeves, G. D., & Koskinen, H. E. J. (2007). Differences in geomagnetic storms driven by magnetic clouds and ICME sheath regions. *Geophysical Research Letters*, *34*(2), L02105. https://doi.org/10.1029/2006GL027775

Rakhmanova, L., Riazantseva, M., Zastenker, G., & Šafránková, J. (2015). Modification of small- and middle-scale solar wind structures by the bow shock and magnetosheath: Correlation analysis. *Planetary and Space Science*, *115*, 12–18. https://doi.org/10.1016/j.pss.2015.03.003

Réme, H., Bosqued, J. M., Sauvaud, J. A., Cros, A., Dandouras, J., Aoustin, C., et al. (1997). The cluster ion spectrometry (CIS) experiment. *Space Science Reviews*, *79*, 303–350. https://doi.org/10.1023/A:1004929816409

Rojas-Castillo, D., Blanco-Cano, X., Kajdič, P., & Omidi, N. (2013). Foreshock compressional boundaries observed by Cluster. *Journal of Geophysical Research: Space Physics*, *118*(2), 698–715. https://doi.org/10.1029/2011JA017385

Ruffenach, A., Lavraud, B., Owens, M. J., Sauvaud, J. A., Savani, N. P., Rouillard, A. P., et al. (2012). Multispacecraft observation of magnetic cloud erosion by magnetic reconnection during propagation. *Journal of Geophysical Research: Space Physics*, *117*(A9), A09101. https://doi.org/10.1029/2012JA017624

Russell, C. T., Luhmann, J. G., Odera, T. J., & Stuart, W. F. (1983). The rate of occurrence of dayside Pc 3,4 pulsations: The L-value dependence of the IMF cone angle effect. *Geophysical Research Letters*, *10*(8), 663–666. https://doi.org/10.1029/GL010i008p00663

Salman, T. M., Lugaz, N., Farrugia, C. J., Winslow, R. M., Jian, L. K., & Galvin, A. B. (2020). Properties of the sheath regions of coronal mass ejections with or without shocks from STEREO in situ observations near 1 AU. *The Astrophysical Journal*, *904*(2), 177. https://doi.org/10.3847/1538-4357/abbdf5

Scolini, C., Verbeke, C., Poedts, S., Chané, E., Pomoell, J., & Zuccarello, F. P. (2018). Effect of the initial shape of coronal mass ejections on 3-D MHD simulations and geoeffectiveness predictions. *Space Weather*, *16*(6), 754–771. https://doi.org/10.1029/2018SW001806

Shue, J. H., Song, P., Russell, C. T., Steinberg, J. T., Chao, J. K., Zastenker, G., et al. (1998). Magnetopause location under extreme solar wind conditions. *Journal of Geophysical Research: Space Physics*, *103*(A8), 17691–17700. https://doi.org/10.1029/98JA01103

Smith, C. W., L'Heureux, J., Ness, N. F., Acuña, M. H., Burlaga, L. F., & Scheifele, J. (1998). The ACE Magnetic Fields Experiment. *Space Science Reviews*, *86*, 613–632. https://doi.org/10.1023/A:1005092216668

Takahashi, K., McPherron, R. L., & Terasawa, T. (1984). Dependence of the spectrum of Pc 3-4 pulsations on the interplanetary magnetic field. *Journal of Geophysical Research: Space Physics*, *89*(A5), 2770–2780. https://doi.org/10.1029/JA089iA05p02770

Takahashi, K., Turc, L., Kilpua, E., Takahashi, N., Dimmock, A., Kajdic, P., & Battarbee, M. (2021). Propagation of ultralow frequency waves from the ion foreshock into the magnetosphere during the passage of a magnetic cloud. *Journal of Geophysical Research: Space Physics*, *126*(2), e28474. https://doi.org/10.1029/2020JA028474

Tsurutani, B. T., Gonzalez, W. D., Tang, F., Akasofu, S. I., & Smith, E. J. (1988). Origin of interplanetary southward magnetic fields responsible for major magnetic storms near solar maximum (1978–1979). *Journal of Geophysical Research: Space Physics*, *93*(A8), 8519–8531. https://doi.org/10.1029/JA093iA08p08519

Tsurutani, B. T., Hajra, R., Echer, E., & Gjerloev, J. W. (2015). Extremely intense (SML ≤ -2500 nT) substorms: Isolated events that are externally triggered? *Annales Geophysicae*, *33*(5), 519–524. https://doi.org/10.5194/angeo-33-519-2015

Tsurutani, B. T., Lakhina, G. S., & Hajra, R. (2020). The physics of space weather/solar-terrestrial physics (STP): What we know now and what the current and future challenges are. *Nonlinear Processes in Geophysics*, *27*(1), 75–119. https://doi.org/10.5194/npg-27-75-2020

Tsurutani, B. T., Lakhina, G. S., Verkhoglyadova, O. P., Gonzalez, W. D., Echer, E., & Guarnieri, F. L. (2011). A review of interplanetary discontinuities and their geomagnetic effects. *Journal of Atmospheric and Solar-Terrestrial Physics*, *73*(1), 5–19. https://doi.org/10.1016/j.jastp.2010.04.001

Turc, L., Fontaine, D., Escoubet, C. P., Kilpua, E. K. J., & Dimmock, A. P. (2017). Statistical study of the alteration of the magnetic structure of magnetic clouds in the Earth's magnetosheath. *Journal of Geophysical Research: Space Physics*, *122*(3), 2956–2972. https://doi.org/10.1002/2016JA023654

Turc, L., Fontaine, D., Savoini, P., & Kilpua, E. K. J. (2014). Magnetic clouds' structure in the magnetosheath as observed by Cluster and Geotail: Four case studies. *Annales Geophysicae*, *32*(10), 1247–1261. https://doi.org/10.5194/angeo-32-1247-2014

Turc, L., Ganse, U., Pfau-Kempf, Y., Hoilijoki, S., Battarbee, M., Juusola, L., & Palmroth, M. (2018). Foreshock properties at typical and enhanced interplanetary magnetic field strengths: Results from Hybrid-Vlasov simulations. *Journal of Geophysical Research: Space Physics*, *123*(7), 5476–5493. https://doi.org/10.1029/2018JA025466

Turc, L., Roberts, O. W., Archer, M. O., Palmroth, M., Battarbee, M., Brito, T., & Dandouras, I. (2019). First observations of the disruption of the Earth's foreshock wave field during magnetic clouds. *Geophysical Research Letters*, *46*(2212), 12644–12653. https://doi.org/10.1029/2019GL084437

Turner, D. L., Kilpua, E. K. J., Hietala, H., Claudepierre, S. G., O'Brien, T. P., Fennell, J. F., & Reeves, G. D. (2019). The response of earth's electron radiation belts to geomagnetic storms: Statistics from the Van Allen Probes Era including effects from different storm drivers. *Journal of Geophysical Research*, *124*(2), 1013–1034. https://doi.org/10.1029/2018JA026066

Villante, U., De Paulis, C., & Francia, P. (2011). The transmission of upstream waves to the magnetosphere: An analysis at widely separated ground stations. *Journal of Geophysical Research: Space Physics*, *116*(A6), A06219. https://doi.org/10.1029/2010JA016263

Wilson, L. B. (2016). Low frequency waves at and upstream of collisionless shocks. *Washington DC American Geophysical Union Geophysical Monograph Series* (pp. 269–291). https://doi.org/10.1002/9781119055006.ch16

Winslow, R. M., Lugaz, N., Scolini, C., & Galvin, A. B. (2021). First simultaneous in situ measurements of a coronal mass ejection by Parker solar probe and STEREO-A. *The Astrophysical Journal*, *916*(2), 94. https://doi.org/10.3847/1538-4357/ac0821

Yermolaev, Y. I., Lodkina, I. G., Nikolaeva, N. S., Yermolaev, M. Y., Riazantseva, M. O., & Rakhmanova, L. S. (2018). Statistic study of the geoeffectiveness of compression regions CIRs and sheaths. *Journal of Atmospheric and Solar-Terrestrial Physics*, *180*, 52–59. https://doi.org/10.1016/j.jastp.2018.01.027

Yermolaev, Y. I., Nikolaeva, N. S., Lodkina, I. G., & Yermolaev, M. Y. (2012). Geoeffectiveness and efficiency of CIR, sheath, and ICME in generation of magnetic storms. *Journal of Geophysical Research: Space Physics*, *117*(A9), A00L07. https://doi.org/10.1029/2011JA017139

Yurchyshyn, V., Liu, C., Abramenko, V., & Krall, J. (2006). The May 13, 2005 eruption: Observations, data analysis and interpretation. *Solar Physics*, *239*(1–2), 317–335. https://doi.org/10.1007/s11207-006-0177-3

Zank, G. P., Nakanotani, M., Zhao, L. L., Du, S., Adhikari, L., Che, H., & le Roux, J. A. (2021). Flux ropes, turbulence, and collisionless perpendicular shock waves: High plasma beta case. *The Astrophysical Journal*, *913*(2), 127. https://doi.org/10.3847/1538-4357/abf7c8

Zhou, X., & Tsurutani, B. T. (2001). Interplanetary shock triggering of nightside geomagnetic activity: Substorms, pseudobreakups, and quiescent events. *Journal of Geophysical Research: Space Physics*, *106*(A9), 18957–18968. https://doi.org/10.1029/2000JA003028